



RESEARCH REPOSITORY

This is the author's final version of the work, as accepted for publication following peer review but without the publisher's layout or pagination.

The definitive version is available at:

<https://doi.org/10.1016/j.gca.2018.11.034>

Román, N., Reich, M., Leisen, M., Morata, D., Barra, F. and Deditius, A.P. (2018)
Geochemical and micro-textural fingerprints of boiling in pyrite.
Geochimica et Cosmochimica Acta

<http://researchrepository.murdoch.edu.au/id/eprint/42744/>

Copyright: © 2018 Elsevier Ltd.
It is posted here for your personal use. No further distribution is permitted.

Accepted Manuscript

Geochemical and micro-textural fingerprints of boiling in pyrite

Nelson Román, Martin Reich, Mathieu Leisen, Diego Morata, Fernando Barra,
Artur P. Deditius

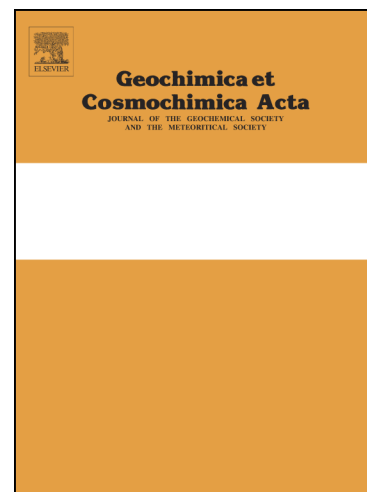
PII: S0016-7037(18)30664-1
DOI: <https://doi.org/10.1016/j.gca.2018.11.034>
Reference: GCA 11029

To appear in: *Geochimica et Cosmochimica Acta*

Received Date: 15 May 2018
Revised Date: 10 October 2018
Accepted Date: 22 November 2018

Please cite this article as: Román, N., Reich, M., Leisen, M., Morata, D., Barra, F., Deditius, A.P., Geochemical and micro-textural fingerprints of boiling in pyrite, *Geochimica et Cosmochimica Acta* (2018), doi: <https://doi.org/10.1016/j.gca.2018.11.034>

This is a PDF file of an unedited manuscript that has been accepted for publication. As a service to our customers we are providing this early version of the manuscript. The manuscript will undergo copyediting, typesetting, and review of the resulting proof before it is published in its final form. Please note that during the production process errors may be discovered which could affect the content, and all legal disclaimers that apply to the journal pertain.



Revised version submitted to *Geochimica et Cosmochimica Acta*

Geochemical and micro-textural fingerprints of boiling in pyrite

Nelson ROMÁN^{1,2*}, Martin REICH^{1,2}, Mathieu LEISEN^{1,2}, Diego MORATA^{1,2}, Fernando BARRA^{1,2} and Artur P. DEDITIUS³

¹Department of Geology and Andean Geothermal Center of Excellence (CEGA), FCFM, Plaza Ercilla 803, Santiago, Chile

²Millennium Nucleus for Metal Tracing Along Subduction, Universidad de Chile, FCFM, Santiago, Chile.

³School of Engineering and Information Technology, Murdoch University, Western Australia 6150, Australia

*E-mail: nroman@ing.uchile.cl

Keywords: pyrite, trace elements, boiling, Cerro Pabellón, geothermal system, epithermal deposit

ABSTRACT

The chemical composition, textures and mineral associations of pyrite provide key information that help elucidate the evolution of hydrothermal systems. However, linking the compositional and micro-textural features of pyrite with a specific physico-chemical process, e.g., boiling versus non-boiling, remains elusive and challenging. In this study we examine pyrite geochemical and micro-textural features and relate these results to pyrite-forming processes at the active Cerro Pabellón Geothermal System (CPGS) in the Altiplano of the northern Chile. We integrate electron microprobe analysis (EMPA) and laser ablation inductively coupled plasma mass spectrometry (LA-ICP-MS) data with micro-textural observations of pyrite and associated gangue minerals recovered from a ~500 m long drill core that crosscuts the argillic, sub-propylitic and propylitic alteration zones of the CPGS. Additionally, we carried out a Principal Component Analysis (PCA) in order to inspect and understand the main data structure of the pyrite geochemical dataset. The concentrations of precious metals (Au and Ag), metalloids (As, Sb, Se, Bi and Tl), and base and heavy metals (Cu, Co, Ni and Pb) in pyrite from the CPGS are significant. Among the elements analyzed, As, Cu and Pb are the most abundant with concentrations that vary from a few parts per

million (ppm) to wt% levels (up to 4.4 wt% of As, 0.5 wt% of Cu and 0.2 wt% of Pb). Based on contemporaneous gangue mineral associations and textures, the mechanisms of pyrite precipitation in the CPGS were inferred. Pyrite formed during vigorous boiling is characterized by relatively high concentrations of As, Cu, Pb, Ag and Au and lower concentrations of Co and Ni compared to pyrite formed under different conditions. These anhedral to euhedral pyrite grains display zones with a porous texture and abundant mineral micro- to nano-inclusions (mainly galena and chalcopyrite) indicating a formation by rapid crystallization. In contrast, pyrite formed under gentle boiling (more gradual cooling and less abrupt physico-chemical variations than in vigorous boiling) to non-boiling conditions is characterized by a higher concentration of Co and Ni, and relatively low concentrations of As, Cu, Pb, Ag and Au. Texturally, these pyrites form aggregates of euhedral and pristine pyrite crystals with scarce pores and mineral inclusions suggesting formation under steadier physico-chemical conditions. Our results show that pyrite can not only record the chemical evolution of hydrothermal fluids, but can also provide critical information related to physico-chemical process such as boiling and phase separation. Since boiling of aqueous fluids is a common phenomenon occurring in a variety of pyrite-forming environments, e.g., active continental and seafloor hydrothermal systems, and porphyry Cu-epithermal Au-Ag deposits, pyrite compositional and textural features are a valuable complement for discriminating and tracking boiling events in modern and fossil hydrothermal systems.

1. INTRODUCTION

In the last decades, several studies have shown that the composition and micro-textures of pyrite are valuable complements to other geochemical information used to elucidate the evolution of hydrothermal systems (Wells and Mullens, 1973; Fleet et al., 1989; Cook and Chryssoulis, 1990; Reich et al., 2005; Large et al., 2009; Muntean et al., 2011; Deditius et al., 2014; Gregory et al., 2016; Tardani et al., 2017). Pyrite is a ubiquitous and abundant sulfide in ore deposits, and several geochemical studies have highlighted its role as a major Au-bearing phase and scavenger of metals and metalloids. Most notably, pyrite has been used as a geochemical tracer in a wide variety of hydrothermal ore deposits including orogenic, sediment-hosted Carlin-type, epithermal Au deposits, volcanic-massive sulfide (VMS), porphyry Cu and iron-oxide apatite (IOA) deposits (Cook and Chryssoulis, 1990; Fleet et al., 1993; Huston et al., 1995; Simon et al., 1999; Vaughan and Kyin, 2004; Reich et al., 2005, 2006, 2013, 2016; Large et al., 2009, 2014; Cook et al., 2009a; Deditius et al., 2009a,b, 2011, 2014; Koglin et al., 2010; Franchini et al., 2015; Gregory et al., 2015a; Deditius and Reich, 2016; Tanner et al., 2016; Keith et al., 2018). These studies have provided not only a

better understanding of metal speciation and partitioning during mineral precipitation, but also have illustrated how physico-chemical processes drive changes in trace element distributions during superimposed events, including hydrothermal alteration, metamorphism and/or associated deformation (Large et al., 2007; Cook et al., 2009a; Thomas et al., 2011; Reich et al., 2013; Deditius et al., 2014; Steadman et al., 2015; Meffre et al., 2016).

A plethora of studies have shown that pyrite can host appreciable concentrations of Au, Ag, Cu, Pb, Zn, Cd, Mn, Co, Ni, As, Sb, Se, Te, Hg, Tl and Bi. Additionally, it has been noted that metal and metalloids can occur as structurally-bounded elements or forming micro- to nano-scale mineral inclusions within pyrite (Reich et al., 2005; Deditius et al., 2008, 2009a,b, 2011, 2014; Deditius and Reich, 2016). Since pyrite composition is strongly influenced by environmental conditions, its geochemical signature reflects the selective partitioning of elements during pyrite growth and ultimately, the composition and physico-chemical nature of the ore-forming fluids and/or marine pore waters (e.g., Deditius et al., 2009a, 2014, Reich et al., 2013; Gregory et al., 2014, 2015a; Large et al., 2014, 2015; Tardani et al., 2017). Furthermore, the significant diversity of textural features in pyrite has been investigated in detail. A large amount of our current knowledge derives predominantly from textural interpretations in orogenic Au systems (Large et al., 2007, 2009; Cook et al., 2013; Gregory et al., 2016), sediment-hosted Au deposits (Large et al., 2014, 2015), VMS (Maslennikov et al., 2009, 2017; Genna and Gaboury, 2015; Wohlgemuth-Ueberwasser et al., 2015; Keith et al., 2016; Melekestseva et al., 2017; Soltani Dehnavi et al., 2018), porphyry-Cu (e.g., Reich et al., 2013; Franchini et al., 2015) and epithermal Au-Ag deposits (e.g., Franchini et al., 2015; Tanner et al., 2016; Kouhestani et al., 2017; Sykora et al., 2018). These studies have shown that pyrite textures can record physico-chemical conditions during precipitation, such as supersaturation or near-equilibrium crystallization, as well as post-formational events, i.e., deformation, dissolution-reprecipitation and recrystallization processes (Cook et al., 2009a).

Recently, the well documented variations in chemistry and texture of pyrite have been linked to changes in fluid composition related to abrupt changes in P-T-X conditions (e.g., Peterson and Mavrogenes, 2014; Tanner et al., 2016; Sánchez-Alfaro et al., 2016; Tardani et al., 2017). However, the controls over the pyrite composition and distribution of trace elements are not well understood. For example, the presence of finely spaced multiple growth zones in pyrite has been interpreted as the result of intermittent excursions of magmatic vapor, changes in internal overpressure and/or externally-forced disturbances such as earthquakes, which can dramatically affect the composition of hydrothermal fluids. Also, processes such as cooling, fluid mixing and boiling have been invoked to explain the compositional variability of pyrite. However, linking the

chemical and textural features of pyrite with a single physico-chemical process remains unconstrained and challenging, in part, due to the scarcity of pyrite data in shallow crustal circulation systems such as geothermal systems and epithermal Au-Ag deposits, where boiling is a common mechanism of sulfide and Au precipitation. In these systems, pyrite is widely distributed and can be associated with different types of hydrothermal alteration assemblages formed at various temperatures, under boiling and non-boiling conditions (Simmons et al., 2005; Libbey and Williams-Jones, 2016; Tardani et al., 2017).

Pyrite is by far the most common sulfide in active geothermal systems including Salton Sea in California (Skinner et al., 1967; McKibben and Elders, 1985; McKibben et al., 1988a,b; Hulen et al., 2004), Rotokawa, Ngawa and Broadlands-Ohaaki in New Zealand (Krupp and Seward, 1987, Cox and Browne, 1995, Simmons and Browne, 2000), Kirishima and Yanaizu-Nishiyama in Japan (Shoji et al., 1989, 1999), Baranskiy and Pauzhetka in Russia (Rychagov et al., 2000, 2009), Los Azufres in Mexico (González-Partida, 2001), Mataloko in Indonesia (Koseki and Nakashima, 2006a,b); Joaquina in Guatemala (Libbey et al., 2015), Reykjanes in Iceland (Libbey and Williams-Jones, 2016) and Tolhuaca in Chile (Tardani et al., 2017). Despite its ubiquitous occurrence, geochemical data of pyrite have been reported only for a few geothermal systems (Shoji et al., 1989, 1999; Koseki and Nakashima, 2006a,b; Rychagov et al., 2009; Libbey and Williams-Jones, 2016; Tardani et al., 2017). These studies have mostly focused on the use of pyrite geochemistry to explore the geological and hydrogeochemical evolution of each particular system, which are mediated to a large extent by the nature and physico-chemical properties of the mineralizing fluids (e.g., temperature, pH, physical state and chemical composition) and host rocks (e.g., permeability and whole-rock chemical composition). Hence, detailed information about textural features of pyrite from active continental geothermal systems is limited, and links to its geochemical signature have not been explored. This is of utmost importance because pyrite from young and active geothermal systems shows fewer growth zones and/or chemical oscillations associated with discrete boiling and fluid mixing events (Tardani et al., 2017), which provide crucial information to interpret the reported complex zoning of pyrite in ore deposits (e.g., Reich et al., 2013; Tanner et al., 2016). This is mostly due to the fact that pyrite in ore deposits records a time-integrated sequence of fluid flow episodes, hindering the accurate identification of major precipitation events.

Here we examine the relation between pyrite geochemistry and micro-textures in order to constrain the pyrite-forming processes at the active Cerro Pabellón Geothermal System (CPGS) in the Altiplano of the northern Chile. The CPGS hosts a high-enthalpy metal-rich geothermal system that has been drilled to ~2 km depth, offering a unique opportunity to evaluate the impact of

physico-chemical conditions on pyrite compositional and textural features, principally the impact of phase-change processes, e.g., boiling, and associated variations in parameters such as temperature, pH and fluid composition. We integrate micro-analytical data with micro-textural observations of pyrite and associated gangue minerals recovered from a ~500 m long drill core that crosscut the argillic, sub-propylitic and propylitic alteration zones of the CPGS. The major, minor and trace element contents of pyrite were determined using a combination of electron microprobe analysis (EMPA) and laser ablation inductively coupled plasma mass spectrometry (LA-ICP-MS). Additionally, we performed a Principal Component Analysis (PCA) to inspect and understand the main data structure of the pyrite geochemical dataset. This statistical analysis confirms that the geochemical features of pyrite are strongly dependent on the depositional conditions at the CPGS. Our data provide an explanation for the observed compositional differences between different pyrite types, and relate specific pyrite-bearing assemblages to vigorous boiling and gentle- to non-boiling mineralization events.

2. GEOLOGICAL BACKGROUND

The Cerro Pabellón Geothermal System (CPGS), formerly known as the Apacheta Geothermal System (Urzúa et al., 2002), is an active geothermal system located 105 km from the city of Calama and 55 km from the El Tatio Geothermal Field, in northern Chile (Fig. 1A). The high-enthalpy CPGS was discovered by Codelco in 1998 during drilling of a shallow water exploration well (PAE-1; Urzúa et al., 2002). Currently, the CPGS geothermal resource is being harnessed by the 48 MW Cerro Pabellón Geothermal Power Plant (ENEL Green Power-ENAP joint venture), the first geothermal power plant in South America, which began operation in 2017.

The CPGS is located within the Central Volcanic Zone (CVZ) of Chile, and is associated with the Altiplano-Puna Volcanic Complex (APVC; de Silva, 1989). A magmatic, high-temperature heat source has been proposed for the CPGS, based on petrological, geophysical and fluid geochemistry evidence (Urzúa et al., 2002; Aguilera et al., 2006, 2008; Tassi et al., 2009, 2010; Piscaglia, 2012). The geology of the area is dominated by the Apacheta-Aguilucho Volcanic Complex (AAVC, Mercado et al., 2009; Piscaglia, 2012), dacitic domes (Chac Inca and Pabellón) and rhyolitic, dacitic and andesitic lava flows (Fig. 1B). The AAVC is located west of Pampa Apacheta, a flat-floored valley where the Cerro Pabellón Power Plant is located. The Pabellón Dome was emplaced over the trace of the northern fault of the NW-SE-trending Pabelloncito Graben, which also hosts the main zone of the geothermal system. The only visible geothermal

surface manifestations are two high-temperature fumaroles and bubbling pools, which occur near the summit of the Apacheta volcano (Fig. 1C).

The geology of the area was first described by Ramírez and Huete (1981), and the evolution of the Apacheta-Aguilucho Volcanic Complex was studied by Mercado et al. (2009) and Piscaglia (2012). The Plio-Pleistocene Apacheta volcano is characterized by andesitic to rhyolitic lava flows and pyroclastic deposits, whereas the Pleistocene Aguilucho volcano is mainly represented by dacitic lava flows. The last manifestation of volcanism in the area corresponds to the Chac-Inca and Pabellón dacitic domes (80-130 ka based on $^{40}\text{Ar}/^{39}\text{Ar}$ dating; Renzulli et al., 2006). The CPGS is hosted in an andesitic to dacitic volcanic sequence, which comprises hydrothermally altered lava flows, volcanic breccias and tuffs (GDN, 2011). Hydrothermal alteration in the system is profuse. Urzúa et al. (2002) reported that argillic alteration associated with the Apacheta fumaroles is the only superficial alteration associated with the active geothermal system at depth. Based on XRD mineralogy, petrographic observations and SEM-EDX analyses of samples from two boreholes (PEXAP-1 and CP-1, Fig. 1B, C and D), Maza et al. (2018) recognized three main hydrothermal alteration assemblages in the system, from top to bottom: argillic, sub-propylitic and propylitic alterations (Fig. 1D). The argillic zone is characterized by a pervasive alteration represented by smectite, zeolites, hematite, calcite and silica. The sub-propylitic alteration zone is dominated by corrensite + chlorite, with albite, quartz, calcite, hematite, stilbite and laumontite. Finally, the propylitic alteration zone is characterized by illite + chlorite, with epidote, titanite, albite, adularia, quartz, calcite, pyrite and chalcopyrite.

A 400-m thick low-resistivity layer, detected by a magnetotelluric (MT) geophysical survey, has been interpreted as the cap-rock of the geothermal system (Fig 1C; Urzúa et al., 2002). Maza et al. (2018) proposed that this impermeable seal layer comprises argillic- and subpropylitic-altered rocks. This could explain the absence of well-developed hydrothermal alteration in rocks above this clay-cap, and the scarcity of geothermal surface expressions, allowing to define the CPGS as a blind geothermal field.

2. SAMPLES AND METHODS

Twenty representative samples from the argillic, sub-propylitic and propylitic alteration zones of the CPGS were selected at different depths from the PEXAP-1 drill core (561.4 m; Fig. 1D). Each sample was inspected and characterized using polarized light and scanning electron microscopy techniques. A subset of eight representative pyrite-bearing samples was selected for

subsequent sulfide compositional analysis (samples BA20, BA21, BA27, BA30, BA31, BA33, BA34 and BA48, Fig. 1D).

2.1 SEM, EMPA and LA-ICP-MS methods

Scanning electron microscopy (SEM) observations were carried out at the Andean Geothermal Centre of Excellence (CEGA), Universidad de Chile, using a FEI Quanta 250 SEM equipped with secondary electron (SE), energy-dispersive X-ray spectrometry (EDS), backscattered electron (BSE) and cathodoluminescence (CL) detectors. The analytical parameters were: spot-size set to 1 - 3 μm , accelerating voltage of 15 keV, beam intensity of 80 μA , and a working distance of ~ 10 mm. For SEM-CL observations, the methodology proposed by Frelinger et al. (2015) was followed.

Electron microprobe analysis (EMPA) of pyrite grains was performed using a CAMECA SX100 microprobe equipped with five wavelength-dispersive spectrometers at the Lunar and Planetary Laboratory, University of Arizona. Operation conditions were: fully focused beam, 40 degrees take-off angle and beam energy of 15 keV. The beam current was 40 nA for spot analyses and 80 nA for WDS X-ray maps. No evidence of beam damage of pyrite grains was detected during analysis. Elements were acquired using the following analyzing crystals: LLIF for Fe K α , Co K α , Ni K α , Cu K α and Zn K α ; TAP for As L α and Se L α ; PET for S K α , Te L α and Pb M α ; and LPET for Ag L α , Sb L α , Au M α and Bi M β . The standards used included natural and synthetic metals, sulfides, arsenides, tellurides and selenides. Counting time (peak) was 20 s for Fe K α , Co K α , Ni K α , Cu K α , Zn K α , Au M α and Bi M β ; 30 s for S K α , Ag L α , Sb L α and Te L α ; 40 s for Pb M α ; and 50 s for As L α and Se L α . The same (peak) counting time was used for total background readings. Mean detection limits ranged from 0.02 to 0.05 wt% for most analyzed elements. Matrix corrections were performed using the PAP method (Pouchou and Pichoir, 1991).

Laser ablation inductively coupled plasma mass spectrometry (LA-ICP-MS) spot analyses were acquired on selected pyrite grains. LA-ICP-MS analyses were undertaken using a 193 nm ArF excimer laser (Photon Machines Analyte 193) coupled to a quadrupole ICP-MS (Thermo Fisher Scientific iCAP Q) at the Mass Spectrometry Laboratory of the Andean Geothermal Center of Excellence (CEGA), Universidad de Chile. Prior to each analysis session, the ICP-MS was tuned by ablating a NIST SRM 610 glass reference material, to ensure acceptable levels of plasma robustness (i.e., $^{238}\text{U}^+ / ^{232}\text{Th}^+$ between 0.95 – 1.05), oxide production ($\text{ThO}^+ / \text{Th}^+ < 0.5\%$) and double-charged production ($^{22}\text{M}^+ / ^{44}\text{Ca}^{++} < 0.01\%$). Ablation was carried out using a laser pulse frequency of 4 Hz, an energy density of ~ 1.5 J/cm 2 , and a spot size of 30 μm in most cases. The laser spot size was

reduced to 20 μm when analyzing small grains, or to avoid ablating visible mineral inclusions. Pure He was used as carrier gas. Each spot was ablated for 30 s following 30 s of gas background collection. The following isotopes were monitored: ^{34}S , ^{51}V , ^{52}Cr , ^{53}Cr , ^{55}Mn , ^{57}Fe , ^{59}Co , ^{60}Ni , ^{63}Cu , ^{65}Cu , ^{66}Zn , ^{69}Ga , ^{72}Ge , ^{73}Ge , ^{75}As , ^{77}Se , ^{82}Se , ^{95}Mo , ^{97}Mo , ^{107}Ag , ^{109}Ag , ^{111}Cd , ^{115}In , ^{118}Sn , ^{120}Sn , ^{121}Sb , ^{123}Sb , ^{125}Te , ^{182}W , ^{197}Au , ^{202}Hg , ^{205}Tl , ^{206}Pb , ^{207}Pb , ^{208}Pb and ^{209}Bi , considering a total quadrupole sweep time of 0.55 s. The calibration procedure considered both external and internal standard calibration (Longerich et al., 1996). The MASS-1 pressed synthetic sulfide reference material (Wilson et al., 2002) was used as the primary standard, and total Fe concentrations obtained previously by EMPA were used as the internal standard. Additionally, the GSE-1G glass reference material (Jochum et al., 2005) was employed as secondary standard for quality control. External standard measurements were performed at the beginning and at the end of each analysis round of 20 spot analyses. Data integration and reduction was carried out using the IoliteTM (v. 2.5) data reduction software (Paton et al., 2011). Caution was taken in the interpretation of irregular signal profiles attributed to mineral or fluid inclusions, or unstable signals produced when ablating thin mineral grains or grain rims. However, and considering that the minimum particle size detectable during LA-ICP-MS profiling was ~ 500 nm, it is possible that in some cases nanometer-sized mineral inclusions affected the overall signal. Additionally, it is important to note that the MASS-1 reference material may contain some heterogeneities, most notably for Au (Wilson et al., 2002). Therefore, LA-ICP-MS depth profiles of the MASS-1 reference material were thoroughly inspected before calibration to avoid introducing Au heterogeneities, and MASS-1 readings were made in duplicates, each time. Therefore, it is expected that the impact of these Au heterogeneities in our data is negligible.

2.2 Statistical analysis

Principal Component Analysis (PCA) was used for a better understanding and interpretation of the pyrite compositional data, including the statistical relationships between the analyzed elements and their variance. Prior to PCA, the probability distribution of each variable (i.e., each analyzed element) was inspected, and a centered log-ratio (CLR) transformation (Aitchison, 1986) was applied afterwards to every variable that approximated to a log-normal distribution (in this case, all considered variables). This procedure overcomes the effects of inherent “closure” of compositional data, i.e., fixed totals of 100 wt% or 10^6 ppm, and approximates each variable to a normal distribution, which is required for PCA (see Reimann et al., 2008). After CLR transformation, data was standardized via calculation of Z-values. A Varimax rotation procedure (Kaiser, 1958) of the principal components was used to improve interpretability of the results.

Rotated PCA solutions are shown via biplots (Gabriel, 1971) where the loadings of each principal component (PC), i.e., the relation between the PCs and the original variables (element concentrations) are represented by arrows. The scores of each PC, i.e., the relation between the PCs and each original data point (individual analysis), are represented by points. The loading of each PC is related to how much a PC explains a variable. High loadings (closer to 1 or -1) indicate that the PC is highly related to the variable. Arrows in biplots indicate, simultaneously, the loadings related to a certain variable on the two PCs considered for each biplot. On the other hand, scores result from the orthogonal projection of each data point onto the extracted PCs. Points in biplots show the scores related to a certain individual analysis on both PCs.

The number of principal components extracted for each PCA was determined as the minimum number of components that explains at least 80% of the total variance of the dataset. Whenever censored data was incorporated into a PCA procedure (i.e., compositional data below detection limit), it was explicitly indicated. In these cases, such data was replaced by half of the detection limit for that element. Nevertheless, only parameters with less than 10% of censored data were considered for PCA. Additionally, scatterplots of raw compositions are used to visualize some of the results. Scatterplots are intended to show unusual structure patterns and how ratios between variables behave in the dataset, and are not used here for assessing correlation between raw composition data. Therefore, when correlation coefficients are shown within scatterplots, they are presented as referential values only.

3. RESULTS

3.1 Sulfide mineral phases

The main sulfide minerals in the analyzed samples are pyrite, chalcopyrite, galena and acanthite (Figs. 2 and 3). Locally, minor chalcocite, covellite, bornite and Cu-bearing sulfosalts were identified. Sulfides are scarce in the upper section of the drill core, which corresponds to the clay-cap zone of the system (Fig. 1D). In this zone, only minor chalcocite and covellite were observed, exclusively within amygdals of the volcanic host rock. No pyrite or chalcopyrite were detected in samples from this zone. A sharp increase in the sulfide abundance was noticed at ~490 m depth, associated with a change in the hydrothermal alteration mineral assemblage from sub-propylitic to propylitic. Pyrite and chalcopyrite are abundant in this portion of the drill core, with galena and acanthite identified in some samples (Figs. 3C and D). Bornite and Cu-bearing sulfosalts occur only as minor phases associated with chalcopyrite, especially in the deepest portion of the drill core (>548 m depth), where pyrite is absent.

Pyrite, the dominant sulfide in the CPGS, is present as euhedral to anhedral disseminated grains, occurring within or adjacent to veinlets, and to a lesser extent in amygdales and vugs, and as a replacement mineral of primary magnetite (Fig. 3B). Chalcopyrite also occurs in veinlets and in amygdales, as well as disseminated in the host rock. Chalcopyrite is mainly associated with late (pyrite-free) calcite veinlets, and to a lesser extent, with late quartz + adularia + (pyrite) veinlets, where it precipitated within open spaces after pyrite formation.

A distinct feature of pyrite and chalcopyrite grains from the CPGS is the ubiquitous presence of micrometer-sized mineral inclusions. These inclusions are observable under polarized reflected light and SEM and consist mainly of galena (Fig. 2A, C, D, and Fig. 3A, B), chalcopyrite (Fig. 2C), and acanthite (Fig. 3A). Additionally, a few Cu-Sb-As-bearing inclusions were detected in some chalcopyrite grains. The presence and nature of inclusions was also inferred by inspection and analysis of the time vs. intensity LA-ICP-MS depth profiles (see Discussion section).

3.2 Pyrite groups

Pyrite from the CPGS can be classified based on its association with different veinlet generations and gangue minerals (Figs. 4 and 5). Three main groups are recognized: Group I is characterized by pyrite that is mainly associated with colloform silica + Fe-oxide crustiform bands (Fig. 4A). The silica has Fe impurities detected by SEM-EDS analyses, and a red jasper-like appearance in hand sample. Group II is characterized by pyrite associated with crustiform bands of colloform silica + mosaic (jigsaw) quartz and zoned quartz + sub-rhombic adularia veinlets (Fig. 4B, C and D). In Group III, pyrite is exclusively associated with zoned quartz + sub-rhombic adularia veinlets (Fig. 4E and F). In some cases, quartz developed comb-like textures when crystallized in open spaces. There is no apparent change in veinlet abundance with depth in the analyzed core. These three pyrite groups occur simultaneously within the same section of the analyzed drill core.

Based on veinlet cross-cutting criteria, a relative sequence can be established for these pyrite groups (Fig. 5). The colloform silica + Fe-oxide banding that characterizes Group I predates Groups II and III, whereas the zoned quartz + adularia veinlets of Group II postdate the colloform silica + mosaic quartz events of the same group. The zoned quartz + sub-rhombic adularia veinlets of Group III are similar to the latest veinlet event of Group II. Thus, Group III and the late event of Group II appear to be synchronous. Therefore, from the earliest to the latest event, pyrite groups are paragenetically arranged as I, II and III, with a partial temporal overlap between Groups II and III.

Despite identification of two different events in Group II, it is difficult to accurately associate the pyrite mineralization with exclusively one of these.

A late, post-Group III event of base- and precious metal sulfide mineralization was observed in the studied samples (Fig. 3C, D and Fig. 4E). This event, characterized by chalcopyrite, galena and acanthite, is closely associated with rhombic calcite precipitation in open spaces, and it is considered the latest mineralization event recognized in the propylitic alteration zone (Fig. 5). This event is best represented in sample BA-20, which marks the transition between the sub-propylitic and propylitic alteration zones (~490 m depth).

3.3 Textural features of pyrite groups

Pyrite from Groups I, II and III, i.e., pyrite-I, -II and -III, respectively, display the following distinct textural characteristics:

Pyrite-I occurs as elongated and relatively large (500 μm - 1 mm) anhedral to euhedral grains and aggregates, usually in close relation with adjacent colloform silica and Fe-oxide bands (Fig. 2 and Fig. 4A). The main feature of pyrite-I is its porous texture, represented by areas with clustered pores and abundant mineral inclusions, and areas of pristine pyrite, without visible inclusions or pores (Fig. 2A and C). Pores are commonly filled with Si-bearing phases. The porous textures of some pyrite grains from this group resemble sieve or corrosion-like textures. Irregular fractures are observed in some grains, and in some fractured areas, chalcopyrite and clustering of galena inclusions are noticed (Fig. 2D). It is common to observe pyrite aggregates with irregular rims at the contact with Fe-oxides or silica-rich colloform bands, and sharp, straight pyrite rims on the opposite side (Fig. 2B and 4A), suggesting that pyrite growth started from the irregular edge and developed perpendicular to banding.

Pyrite-II grains are subhedral to euhedral (10 – 200 μm ; Fig. 3A and B) with some showing zones with abundant pores and mineral inclusions, similar to those described in pyrite-I. These areas are located preferentially in the cores of pyrite grains, whereas the external zones of the same grains are generally pristine, with scarce pores and inclusions (Fig. 3A and B). Some pyrite grains from this group have irregular fractures, but not to the same degree as in pyrite-I.

Pyrite-III displays isolated to clusters of subhedral to euhedral crystals, characterized by morphologies dominated by cubic and pyritohedral shapes, with sizes between 20 and 500 μm (Fig. 3C, D and Fig. 4E, F). Pyrite grains from this group have scarce pores or no porosity at all, are less fractured than pyrite-I and II, and are usually surrounded by late chalcopyrite, galena and/or acanthite.

3.4 Chemical composition of pyrite

All EMPA and LA-ICP-MS analyses are reported in Appendices A and B, respectively, whereas statistical parameters for the dataset are shown in Figure 6. It is important to note that analyses were performed on clean pyrite areas with no visible mineral inclusions. However, and considering that discrete nano-inclusions and/or clusters of mineral nanoparticles are not fully resolvable by LA-ICP-MS during depth profiling, it is likely that some analyses may have been affected by the ablation of mineral inclusions within pyrite (i.e., irregular, “spiky” profiles). Therefore, and in order to evaluate this effect, the entire dataset is displayed in Figure 6 as white boxes, whereas inclusion-free LA-ICP-MS analyses are shown in grey, i.e., those analyses that did not show any visible evidence of mineral inclusions (e.g., flat profiles). Additionally, concentrations determined by EMPA are higher than those determined by LA-ICP-MS due to the higher detection limit of the EMP analyses. Moreover, EMPA data for Zn, Te and Au are possibly affected by mineral nano- to micro-inclusions, explaining the discrepancy between EMPA and LA-ICP-MS data for these elements.

Inspection of the entire LA-ICP-MS database reveals that pyrite from the CPGS is enriched in minor and trace elements, where Cu, Pb, As and Ag reach maximum concentrations of >1 wt%. However, concentrations of the aforementioned elements are highly variable, in particular for Pb and Ag, spanning five orders of magnitude from sub- ppm values to >1 wt%. Au concentrations are also high, reaching up to 179 ppm with a median concentration of 1.7 ppm. It is likely that some minor and trace element concentrations measured in pyrite are influenced by the presence of mineral sub-micron inclusions. This seems to be more evident for Pb, Au and Ag, where maximum concentrations can be up to two orders of magnitude higher than in the inclusion-free data (Fig. 6).

Overall, the inclusion-free data are consistent with the total database (Fig. 6, gray boxes). Pyrite from the CPGS is characterized by high concentrations of As, Cu and Pb, with up to ~4.4, ~0.5 and ~0.2 wt%, respectively. These elements were detected in almost all analyzes (Fig. 6 and Appendix B). As shows the highest median concentration of all the analyzed elements, 0.10 wt%. Co, Ni, Sb, Se and Ag were also detected in most analyzes, showing concentrations spanning three to four orders of magnitude, and maximum values of 0.05, 0.12, 0.09, 0.11 and 0.10 wt%, respectively. Among the elements showing the lowest concentrations, Bi, Au and Tl were detected in more than a half of the analyzes, reaching maximum concentrations of 39, 14 and 62 ppm, respectively. Zn, Hg and Te were detected in a few grains, with concentrations <1000 ppm for Zn, <100 ppm for Hg and <10 ppm for Te. V, Cr, Mn, Ge and W were detected in less than half of the analyzes. Among these elements, Mn shows the highest concentration, reaching a maximum of 242

ppm, whereas the remaining elements show concentrations of less than 30 ppm. Ga, Sn, Mo, Cd and In have concentrations below 10 ppm, with the exception of Cd that displays a maximum of 36 ppm.

Minor and trace element concentrations in pyrite groups

In order to avoid the potential chemical bias introduced by mineral inclusions, only the inclusion-free data were used to differentiate pyrite Groups I, II and III (Fig. 7). In all groups, As is present in the highest concentration, however, major compositional differences arise between these groups, especially between pyrite-I and -III.

Pyrite-I displays the highest median concentrations of Cu, Pb, As, Au and Ag, and the lowest median for Ni and Co contents (yellow boxes in Fig. 7). In contrast, pyrite-III shows the highest median Ni concentration, a Co median concentration higher than in pyrite-I, and the lowest median of Cu, Pb, As, Sb, Bi, Au, Ag and Tl concentrations (white boxes in Fig. 7). Pyrite-II has the highest median for Sb, Bi and Tl, high Co concentrations similar to pyrite-III and intermediate median concentrations for the other analyzed elements (blue boxes in Fig. 7). Se concentrations are similar in all groups. It is important to note that the concentration range of the analyzed elements, i.e., maximum and minimum values, can be similar between pyrite groups. However, the concentration distribution can significantly vary, as evidenced by, e.g., Cu (median concentration of Cu is higher in pyrite-I than in pyrite-II and III, but the concentration range is similar in all three, Fig. 7).

Pyrite WDS X-ray maps

The WDS X-ray maps for selected elements in pyrite grains are shown in Figures 8, 9 and 10.

Pyrite-I grains show a distinct compositional zoning, where As-Cu-rich growth bands alternate with As-Cu-poor zones (Figs. 8B and C). The most external growth zone of these pyrite grains is depleted in these elements. The As-Cu rich zones are well-defined in pristine pyrite areas and are more diffuse in porous and inclusion-rich areas (e.g., Fig 8D and E). Additionally, As-poor zones with abundant chalcopyrite inclusions are observed (Fig. 8A, B and C), and in a single grain from this pyrite group, a thin Co-rich band was detected between an As-rich zone and the As-depleted outermost rim.

Pyrite-II grains have a different zoning pattern, consisting of well-defined As, Cu and Co zones (Fig. 9). All analyzed pyrite grains from this group are characterized by two or three

compositional zones. From core to rim, these are: (a) Cu-(Co)-rich zones with relatively moderate contents of As; (b) As-rich, Co-poor zones, with relatively moderate contents of Cu; and (c) rims depleted in both As and Cu, similar to the outermost rims in pyrite-I grains (Fig. 8). Zone (a) may be absent (Fig. 9E), while zone (b) and depleted rims (c) are common in all mapped grains from this group. Zone (a) may show, in turn, zoning where As and Cu are geochemically decoupled (Fig. 9J and K). The grain shown in Figure 9E-H corresponds to a particular case where Cu zoning is not detected and As is enriched in the core. This grain corresponds to a pyrite-II subgroup which is associated with the highest concentrations of As, Sb and Hg in the pyrite-II dataset, coupled with the highest Sb/Pb ratios as shown in the elemental scatter plots (Fig. 11F). Furthermore, a thin Co-enriched band between zones (b) and (c) was identified in some grains (e.g., Fig. 9H). The galena inclusions shown in Figure 9I are almost completely contained in compositional zone (a). Zones (b) and (c) are also characterized by sharp outlines.

In contrast, the WDS X-ray maps of pyrite-III grains (Fig. 10) do not display well-defined compositional zoning patterns such as the observed for As in pyrite-I and II grains. As is homogeneously low in pyrite-III, whereas the high Cu and Co zones are mainly related to later interstitial galena and acanthite, minerals which are relatively enriched in both metals (Fig. 10).

Elemental scatter plots

Elemental concentration scatter plots for Co-Ni, Co-Cu, Co-As, Au-As, Cu-As, Sb-Pb, Ag-Pb, Bi-Sb and Tl-Sb are shown in Figure 11, considering only inclusion-free data. Co displays a positive correspondence with Ni (Fig. 11A), with almost all Co/Ni ratios between 0.1 and 10, and most commonly between 1 and 10. Co/Ni ratios for pyrite-III display a more scattered pattern than the other two groups, and correspond to the lowest Co/Ni ratios of the dataset. The Co/Ni ratios of pyrite-I are slightly higher than in the other groups. Co shows a scattered pattern when plotted against Cu and As (Figs. 11B and C, respectively). As, on the other hand, shows a weakly positive and scattered trend with Au and Cu (Figs. 11D and E, respectively).

Positive trends were found for Sb-Pb (Fig. 11F), Ag-Pb (Fig. 11G), Bi-Sb (Fig. 11H) and Tl-Sb (Fig. 11I), with all of these elements showing similar behavior. The Sb vs. Pb scatter plot displays, for almost all samples, a very consistent Sb/Pb ratio that spans the entire concentration range of both elements, close to $Sb/Pb = 0.1$. However, a pyrite-II subgroup deviates and shows a $Sb/Pb > 0.5$. Pyrites from this subgroup are also relatively enriched in As, Tl and Hg. The higher Ag/Pb ratios, on the other hand, correspond, to a great extent, to pyrite-I. Pyrite Bi/Sb ratios are

mainly between 1 and 0.01, and Tl/Sb ratios are mostly between 0.1 and 0.01, with no visible differences between veinlet associations.

4. DISCUSSION

4.1 Incorporation of metals and metalloids in pyrite

Analyzed pyrite grains from the CPGS can be classified as “arsenian” in terms of their As content reaching up to ~4 wt% (Figs. 6 and 7). WDS compositional maps (Fig. 8B and E, Fig. 9B, F and J, and Fig. 10B and F) show that the distribution of As is relatively homogeneous in each pyrite zone, suggesting that As is structurally bound within pyrite. The As-Fe-S ternary diagram (Fig. 12A) and the As vs. S scatterplot (Fig. 12B) suggest that As^{-1} dominantly substitutes for S in pyrite. This is confirmed by the flat ^{75}As spectrum in depth-profiles shown in Figure 13, which are in agreement with a solid solution mode of As incorporation. However, the As-Fe-S ternary diagram (Fig. 12A) suggests the (minor) occurrence of As^0 nano-inclusions (Deditius et al., 2009a) in pyrite-I and II, a feature previously reported for pyrites from the Tolhuaca Geothermal System, Chile (Tardani et al., 2017). There is no clear evidence of the occurrence of As^{2+} -pyrite or As^{3+} -pyrite in the CPGS, nonetheless this cannot be ruled out as data clustering close to stoichiometric pyrite composition may hide these substitutional trends (Fig. 12A). In addition, the As-Fe-S ternary diagram also indicates that substitution of Fe^{2+} by Me^{2+} , where Me represents metallic or similar elements, is a major mechanism for incorporation of trace elements (i.e., Cu, Co, Ni, Pb and Ag) in pyrite from the CPGS (Figs. 6 and 7).

The Cu content in pyrite from the CPGS (up to ~1 wt%) is related to two different mineralogical forms, which are observable in the WDS X-ray maps (Figs. 8, 9 and 10): (i) structurally bound Cu, and (ii) micrometer-sized Cu-bearing inclusions, mainly chalcopyrite. Structurally bound Cu is represented in WDS maps by the relatively uniform dark-blue color of pyrite grains, and by homogeneously-distributed, higher intensity Cu-bearing zones. The negative trend between Cu and Fe (EMPA data, Appendix A) indicates that substitution between Fe^{2+} and Cu^{2+} is the most likely mechanism for Cu incorporation into pyrite structure. Cu-bearing inclusions, on the other hand, are shown as discrete high-intensity zones in WDS maps (e.g., Fig. 8C and F, and Fig. 9K). The Cu-bearing inclusions shown in Figure 8A and C are chalcopyrite, which is the most common Cu-sulfide inclusion in pyrite (Reich et al., 2013). Late chalcopyrite precipitated into pyrite fractured areas (e.g., lower-right zone, Fig. 8C) can be differentiated from inclusions that are visible in the center-left zone of the same map. In addition, galena inclusions also bear appreciable Cu (and Co) contents, as suggested by WDS maps (Fig. 8D and F, Fig. 9I and K, and Fig. 10).

Furthermore, the two mineralogical forms of Cu in pyrite can be inferred from LA-ICP-MS depth profiles, where structurally bound Cu is inferred from a flat profile (Fig. 13C), and Cu-bearing inclusions from spikes in the ^{63}Cu signal (Fig. 13D). Cu-bearing inclusions are more common in pyrite-I in comparison with the other two groups of pyrite.

The WDS X-ray maps (Fig. 9D, H and L, and Fig. 10D and H) and the representative ^{59}Co intensity vs. depth LA-ICP-MS profile (Fig. 13C) show that Co occurs as a structurally bound element within pyrite. The strong positive correspondence between Co and Ni suggests that this is also the case for Ni (Fig. 11A). Most of the EMPA data for Co and Ni are below detection limits and Fe was used as an internal standard for laser ablation measurements, hence a proper evaluation of the substitution mechanism of these two elements in the pyrite structure was unfeasible. Regardless, it is likely that Co substitutes extensively for Fe in pyrite because both have similar ionic radii and a structural affinity exists between pyrite and the CoS_2 end-member (Vaughan and Craig, 1978; Tossell et al., 1981; Abraitis et al., 2004; Gregory et al., 2015a, b). As pointed out above, galena bears appreciable contents of Co (Fig. 10D and H), indicating that Co may also occur incorporated in discrete galena inclusions in pyrite, particularly in pyrite-I and II.

Co/Ni ratios in pyrite from CPGS are between 0.1 and 10 for most analyzed spots, with the majority of the data showing Co/Ni between 1 and 10, which is characteristic of pyrite of hydrothermal origin (Bajwah et al., 1987; Gregory et al., 2015a; Reich et al., 2016, and references therein). Overall, there is a systematic decrease in Co/Ni ratios from pyrite-I to III, with pyrite-II displaying intermediate ratios. Compositional data of pyrite groups (Fig. 7) show that this difference may be due to an enrichment of Ni with respect to Co from pyrite-I to III. Co and Ni concentrations in the CPGS are relatively lower than in other geothermal systems, such as Tolhuaca (Tardani et al., 2017), and Mataloko (Koseki and Nakashima, 2006a, b), but similar to Kirishima (Shoji et al., 1989) and Pauzhetka (Rychagov et al., 2009) (Fig. 14). The first two systems have been linked to mafic magmatic sources, whereas the volcanic host rocks of Kirishima and Pauzhetka have a relatively more felsic composition, being dominantly andesitic in Kirishima, and andesitic to dacitic in Pauzhetka. This suggests that the hydrothermal system associated with the CPGS is possibly linked to a relatively more felsic source, which agrees with the dominant andesitic to dacitic compositions of the volcanic products that characterize the host rock of the CPGS.

Pb is an abundant trace element in pyrite from the CPGS, i.e., up to ~0.2 wt% and ~9 wt% considering inclusion-free data vs. the entire dataset, respectively. Pb occurs dominantly as micrometer-sized galena inclusions in all three pyrite groups, as evidenced in BSE images (e.g., Figs. 2C and D, 3A and B, 9I and 13A) and in some LA-ICP-MS depth-profiles (Figs. 13B and E).

In depth-profiles, galena inclusions feature coupled peaks of ^{208}Pb and ^{209}Bi , commonly associated with ^{107}Ag . This observation is consistent with positive correspondences between Pb, Ag, Bi and Sb (Fig. 11F, G and H). However, Pb can also occur as a structurally bound element or incorporated as nanometer-sized inclusions that are not resolved by LA-ICP-MS, as evidenced by a flat ^{208}Pb profile (Fig. 13F). A high concentration of structurally bound Pb is associated with high concentrations of As, Sb, Tl and Hg in solid solution (Fig. 13F). The incorporation of Sb and other large anions might promote the incorporation of Pb into the pyrite structure in a similar way as As promotes the incorporation of Au (Reich et al., 2005) in pyrite, or the incorporation of Cu and Ag into sphalerite via coupled substitution associated with In^{3+} or Sb^{3+} (Cook et al., 2009b).

The median concentration of Au and Ag in pyrite from the CPGS (1.7 ppm for Au and 86 ppm for Ag) is notoriously higher (up to one order of magnitude) than in pyrite from other geothermal systems, such as Tolhuaca (Tardani et al., 2017) and Reykjanes (Libbey and Williams-Jones, 2016). The incorporation of Au into pyrite is favored by the structural distortion or by superficial effects caused by the incorporation of cationic or anionic As in pyrite (Simon et al., 1999; Palenik et al., 2004; Deditius et al., 2008, 2014). The solubility curve defined by Reich et al. (2005) for Au in arsenian pyrite illustrates the strong control of As on this element, and show that Au can occur as either a structurally bound element (Au^{+1}) or forming Au^0 nanoparticles. Furthermore, it has been shown that the higher concentrations of Au in pyrite are commonly related to the presence of Au-bearing inclusions (Reich et al., 2005; Deditius et al., 2014; Gregory et al., 2015a). On the other hand, Ag can be incorporated into pyrite as solid solution via substitution of Ag^+ for Fe^{2+} or constituting nano-inclusions of native Ag, electrum, sulfides and sulfosalts within pyrite grains (Huston et al., 1995; Abraitis et al., 2004; Deditius et al., 2011).

At the CPGS, Au and Ag are incorporated into pyrite as both solid solution and mineral inclusions. Ag is associated with different types of inclusions, observable using BSE imaging and by the inspection of the ^{107}Ag and ^{197}Au signal intensities in LA-ICP-MS depth-profiles (Fig. 13). The inclusions have variable compositions including Ag-S (Fig. 13A), Ag-Cu (Fig. 13A), Au-Ag (Fig. 13B) and Au-Ag-(Cu-Se) (Fig. 13E), and Ag-bearing galena (Fig. 13B). Ag-Au-(Cu-Se)-bearing inclusions probably correspond to acanthite, as supported by the WDS compositional maps of Figure 10, which show relatively higher concentrations of Cu in acanthite in relation to the adjacent pyrite. The incorporation of Ag as solid solution is suggested by the flat ^{107}Ag intensity response shown in the LA-ICP-MS depth-profiles (Fig. 13C and F). Au, as noted above, occurs as solid solution and also as Au-Ag-bearing inclusions in pyrite. Au-As analyses (inclusion-free LA-ICP-MS data only) plot under the Au solubility curve defined by Reich et al. (2005) (Fig. 11D),

suggesting that Au in the analyzed spots occurs dominantly as a structurally bound element. This is also supported by the relatively flat ^{197}Au spectrum in the depth-profile (Fig. 13C).

4.2 Interpretation of pyrite and gangue minerals textures

Studies in geothermal systems and epithermal Au-Ag deposits have shown that pyrite can display a large variety of textures, including brecciated, colloform, porous, fibrous and inclusion-rich textures (e.g., Deditius et al., 2009a, b; Franchini et al., 2015; Tanner et al., 2016; Kouhestani et al., 2017). In the CPGS, pyrite grains show several of these textures and morphologies, including porous and inclusion-rich zones, and brecciated subhedral to euhedral pyrite grains (Figs. 2 and 3). Additionally, gangue minerals associated with pyrite, i.e., silica phases, adularia and calcite, can provide key information for the interpretation of the sulfide-forming conditions. In this section, the textural features are interpreted and physico-chemical conditions, including fluid boiling, cooling and/or mixing, are inferred for each pyrite group.

Pyrite I (vigorous boiling): These pyrites have the highest concentrations of As, Au, Ag, Cu and Pb of all analyzed pyrites at the CPGS, and are relatively depleted in Co and Ni (Fig. 7). The close association of elongated pyrite aggregates with adjacent colloform silica bands suggests that pyrite-I formation was synchronous with the development of silica and Fe-oxide banding. The presence of colloform silica, the dominant silica texture in this group, suggests rapid supersaturation of the hydrothermal fluid with respect to amorphous silica, compatible with multiple and vigorous boiling events (cf. Fournier, 1985; Dong et al., 1995; Moncada et al., 2012; Rusk, 2012). This is further supported by early, broken and small rhombic adularia crystals incorporated into late calcite veinlets in sample BA-33 (Pyrite-I), indicating that previous to carbonate precipitation, protracted boiling conditions were dominant during the formation of pyrite-I (cf. Reed and Spycher, 1985; Dong and Morrison, 1995). The clustered mineral inclusions and pores described in pyrite-I grains also point to boiling processes. These textural features are similar to those described at the Dongping Au deposit, China and the Chah Zard epithermal Au-Ag deposit, Iran (Cook et al., 2009a; Kouhestani et al., 2017). Cook et al. (2009a) suggested that areas of clustered pores and telluride inclusions in pyrite from Dongping were formed by a coupled dissolution-reprecipitation process triggered by a percolating fluid under fluctuating $f\text{O}_2$ and $f\text{S}_2$ conditions. A similar mechanism may be responsible for the porous, inclusion-rich zones in pyrite-I from the CPGS, since considerable variations in physico-chemical parameters (e.g., in $f\text{O}_2$ and $f\text{S}_2$, Williams-Jones et al., 2009) are expected during multiple vigorous-boiling events.

Pyrite-II (vigorous boiling to gentle/non-boiling): These pyrites have intermediate concentrations of As, Au, Ag, Cu and Pb in comparison with the other two groups of pyrite from the CPGS, and higher concentrations of Co and Ni compared with pyrite-I (Fig. 7). Pyrite-II textures shares some similarities with pyrite-I. The areas of clustered inclusions and pores found in the cores of some pyrite-II grains suggest that, as for pyrite-I, physico-chemical conditions during pyrite core formation were highly fluctuating. In contrast, the inclusion-free, clean pyrite rims are consistent with steadier physico-chemical conditions. Pyrite-II is associated with colloform and mosaic quartz veinlets, and late zonal quartz + sub-rhombic adularia. The colloform and mosaic (jigsaw) textures of quartz in this pyrite group are also linked to supersaturation with respect to amorphous silica, compatible with vigorous boiling of the parental hydrothermal fluid. In contrast, the presence of zonal quartz and sub-rhombic adularia is related to slower crystallization kinetics and slight supersaturation with respect to quartz and adularia. Considering that adularia is strongly associated with boiling (Browne, 1978; Dong and Morrison, 1995), it is likely that this late event of zonal quartz + sub-rhombic adularia was formed as a result of non-vigorous, gentle boiling conditions transitioning to non-boiling conditions. In summary, the formation of pyrite-II is compatible with a shift from vigorous boiling to gentle- and non-boiling conditions.

Pyrite-III (gentle boiling/non-boiling): These pyrites have the lowest concentrations of As, Au, Ag, Cu and Pb of all analyzed pyrites at the CPGS, and are relatively enriched in Co and Ni, with Co concentrations similar to pyrite-II (Fig. 7). The formation of pyrite-III was related to gentle boiling transitioning to non-boiling conditions, as evidenced by the presence of zonal quartz + sub-rhombic adularia veinlets. Pyrite-III is characterized by euhedral to subhedral cubic and pyritohedron morphologies, which are consistent with direct precipitation from a hydrothermal fluid in open spaces under relatively steady physico-chemical conditions. This interpretation is also supported by the scarcity of areas with clustered pores and inclusions, and by the homogeneous size of pyrite aggregates, suggesting a slower growth. The scarcity of visible mineral inclusions may be related to precipitation of pyrite from a fluid undersaturated with respect to inclusion-forming metals, such as Pb, Ag and Au. This is consistent with the lower concentrations of Pb, Ag, Au and As in pyrite-III (Fig. 7). Pyrite-III was followed by a late event of chalcopyrite, galena, acanthite and rhombic calcite precipitation in open spaces and fractures. The formation of rhombic calcite is compatible with slow kinetics of crystallization and linked to non-boiling conditions (Simmons and Christenson, 1994; Moncada et al., 2012). This late stage mineralization might have been related to mixing of cold, descending CO₂-rich waters with hotter, rising hydrothermal fluids, leading to subsequent base and precious metals precipitation. This is the proposed mechanism responsible for the formation of bonanza ores in carbonate-base metal-Au systems (e.g., Corbett and Leach, 1998),

which shares several similarities with the late chalcopyrite-galena-acanthite-calcite mineralization in the CPGS. In summary, the close association of pyrite-III with the late base- and precious-metal sulfide precipitation stage suggests that these events represent the waning stages of boiling in the studied zone, before its complete cessation.

As an explanatory note, and acknowledging the fact that fluid inclusion studies can provide unequivocal evidence of boiling (Bodnar et al., 1985), we argue that the geochemical, mineralogical and textural features reported here strongly suggest that boiling conditions prevailed during pyrite formation in the CPGS. Additionally, it is important to note that the textural and chemical features of pyrite formed during boiling and reported here, may vary between different hydrothermal environments. For example, in VMS deposits, similar porous textures reported in pyrite are attributed to high-pressure, non-boiling conditions (e.g.: Maslennikov et al., 2009). Therefore, textural and geochemical studies of pyrite should be always accompanied by a detailed geological and mineralogical characterization of the ore-forming environment.

4.3 Processes controlling pyrite geochemistry

Several studies have shown that a wide variety of elements can be incorporated into pyrite from hydrothermal fluids. Structurally-bound incorporation of metals and metalloids can be enhanced by the presence of As in the growing pyrite surface, leading to efficient chemisorption and destabilization of metal complexes (Maddox et al., 1998; Rickard and Luther, 2007; Deditius et al., 2014; Reich et al., 2005, 2013, 2016). Furthermore, addition of metals by local supersaturation of metals, triggered by redox effects on pyrite surfaces (Mikhlin et al., 2011), is linked to the formation of nano- to micro-inclusions of sulfides and native metals (Reich et al., 2006, 2011; Deditius et al., 2011; Hough et al., 2011). This has led to several studies that show how the chemical composition of pyrite can be used to track changes in the evolving hydrothermal fluid (Deditius et al., 2009b, 2014; Reich et al., 2005, 2013, 2016; Tardani et al., 2017).

Different processes have been invoked to explain the variability or changes in the composition of pyrite-forming fluids. In the high-temperature porphyry environment, major compositional changes can be achieved during phase separation of a magmatic-hydrothermal supercritical fluid, owing to selective metal and metalloid partitioning between a low density, vapor-rich fluid and a high density hypersaline liquid (Kouzmanov and Pokrovski, 2012; Reich et al., 2013). In the shallow geothermal and epithermal environments (<1.5 km depth), the mixed influence of pyrite-forming fluids and magmatically-derived As-rich vapors have been proposed to explain the As-Cu decoupling detected in pyrite grains from certain systems such as in the Pueblo

Viejo, República Dominicana and Yanacocha, Perú high-sulfidation Au-Ag epithermal systems (Deditius et al., 2009b) and in the Tolhuaca active geothermal system (Tardani et al., 2017). In submarine hydrothermal systems, on the other hand, mixing between hydrothermal fluids and oxygenated seawater has been suggested to explain the compositional variability in pyrite from black smokers and VMS deposits (Maslennikov et al., 2009; Genna and Gaboury, 2015; Keith et al., 2016). In the continental geothermal environment, processes such as cooling, fluid mixing and boiling have a strong impact on fluid chemistry. The influence of boiling on metal solubility has been investigated by several researchers (e.g., Spycher and Reed, 1989; Simmons and Browne, 2000; Simmons et al., 2016), which have noted a major impact on the depletion of Au, Ag, Pb and Cu in the ascending geothermal fluids. Simmons et al. (2016) noted that not every element is affected in the same manner by boiling, reporting high concentrations of As, Sb and Tl (among others) in fluids that underwent boiling at depth (“boiled waters”). Furthermore, Libbey and Williams-Jones (2016) suggested that pyrite composition from the Reykjanes geothermal system is controlled, at least in part, by boiling processes, based in the observation that the maximum concentrations of pyrite had a clear relation with depth in the system, finding sharp increases in Au, Ag and Pb at depth of the current boiling level in the system.

During boiling in the geothermal and epithermal environment, bubbles of a low-density vapor are released from the aqueous fluids at depth. In contrast to other higher-temperature environments, the metal transport capacity of the vapor is hindered by its low hydration capacity and low density (Pokrovski et al., 2005, 2013; Heinrich, 2007). Because of this, the compositional differences between the different pyrite groups at the CPGS cannot be explained by selective vapor-phase fractionation. Nevertheless, there are elements such as Hg (and As in some cases), that could be easily volatilized and concentrated in the vapor phase (Spycher and Reed, 1989; Pokrovski et al., 2013). Furthermore, the influence of deep and high-temperature As-rich, Cu-poor vapors invading the geothermal reservoir cannot be discarded (Migdisov et al., 2014). However, this process does not seem likely to explain the chemical features of pyrite at CPGS, mainly because pyrite-I grains do not show evidence of As-Cu decoupling (Fig. 8B and C). Furthermore, compositional zoning of pyrite (Fig. 8 and Fig. 9) does not resemble the thin, oscillatory zoning found in pyrite from Pueblo Viejo and Yanacocha (Deditius et al., 2009b). Therefore, and considering the geochemical and textural data presented here, we argue that boiling and cooling processes can be invoked to explain the observed geochemical differences between the pyrite groups from the CPGS.

Both boiling and cooling processes may have a profound effect on metal and metalloid solubility in pyrite-forming fluids. In particular, sharp physico-chemical changes are triggered by

boiling processes, including loss of H_2S , H_2 , CO_2 and other volatiles to the vapor phase, coupled with cooling and pH and $f\text{O}_2$ increase (Simmons and Christenson, 1994; Dong and Morrison, 1995; Simmons and Browne, 2000; Williams-Jones et al., 2009). Such abrupt changes can lead to extensive saturation, thus, the high concentrations of As, Cu, Pb, Ag and Au in pyrite formed under boiling may be the result of the preferential incorporation of metals and metalloids from the pyrite-forming fluids once saturation conditions are met. On the other hand, the relative Co enrichment in pyrite formed under gentle boiling and non-boiling conditions could be related to a greater sensitivity of Co complexes to physico-chemical changes that are not necessarily associated with boiling. It has been shown that cooling may have a dramatic effect on destabilization of Co-chloride complexes in hydrothermal fluids. Specifically, a reduction of temperature from 300 to 200°C can lead to a decrease in Co solubility by up to two orders of magnitude (Migdisov et al., 2011). Finally, differences in the degree of destabilization of metal and metalloid complexes during boiling events could produce elemental fractionation and precipitation in different boiling horizons, depending on the nature of each complex. In particular, As and other metalloids forming hydroxide complexes in solution (e.g., Pokrovski et al., 2013) may be transported further after boiling and destabilized later at shallow or distal levels of the system (e.g., Simmons et al., 2016). This could allow the formation of the As-Sb-Bi-Tl-rich, Cu-depleted pyrite-II subgroup.

We further explore the impact of boiling vs. non-boiling processes on pyrite composition by performing a principal component analysis (PCA) that provides a general overview of the compositional variability in pyrite from the CPGS. This statistical approach has been used successfully to understand trace element concentrations in pyrite from sedimentary environments (e.g., Gregory et al., 2015a). In our analysis, six elements were considered: Co, Ni, As, Cu, Pb and Ag, as these elements have the highest variance and were detected in most spot analyses (Figs. 6 and 7).

We took advantage of the synthesis capability of biplots to show our PCA results (Fig. 15). Biplots can simultaneously display two selected Principal Components (PC, x and y axes of the plots), the analyzed elements (shown as arrows), the individual spot analyses (shown as points), and the relationship between these. This allows visualizing which elements are associated with the largest variance, the degree of correlation between the analyzed elements, and how the original individual analyses relate to analyzed elements in this multivariate space. The interpretation of biplots requires the use of arrow lengths and direction as well as the angles between them. Arrow length is related to how much of the total variance of the element is represented by the displayed PC. A long arrow (high loadings) indicates that a majority of the variance associated with the

represented element is displayed in the biplot, whereas short arrows (low loadings) indicate that the shown PC contains almost no information about the corresponding element. Long arrows aligned with a single PC indicate that the variance of the represented element is almost entirely contained in that PC. The direction of each arrow is related to the direction in which the concentrations of the corresponding element increase, a feature that needs to be coupled with arrow length considerations, as explained above, and that is useful to be evaluated together with data points (scores). Finally, the angle between arrows is associated with the correlation between the analyzed elements. Small angles between arrows (as in near overlapping arrows) indicate a high positive correlation and well constrained ratios between elements. Two orthogonal long arrows suggest that the represented elements are not correlated, and two opposed long arrows represent a high negative correlation and highly variable ratios between these elements.

Two PCA procedures were carried out (Fig. 15). The first PCA was performed omitting below detection limit (BDL) data (Figs. 15A and B), whereas the second considered the BDL data by assigning half of the corresponding detection limit (Figs. 15C and D). In both cases, more than 80% of the variance can be explained with the extraction of three PC. The two PCAs yielded similar results, and the main difference is how Pb is related to other variables. Biplots show an evident clustering of data by pyrite groups, demonstrating their systematic compositional differences, as mentioned above. Pyrite-I data, linked to vigorous boiling, are clustered and associated with the Cu, Pb, Ag and As arrows. Pyrite-III data, on the other hand, are linked to gentle boiling or non-boiling conditions and cluster on the opposite side of the biplots, associated with Co-Ni maxima. Pyrite-II is transitional between pyrite-I and pyrite-III, supporting the idea that, compositionally, this group has intermediate characteristics.

Principal Component 1 (PC1), which corresponds to the horizontal axes in biplots (Fig. 15) and explains ~45% of the total variance of the six elements considered, is closely related to Co, Ni, Ag and Pb in both PCAs. Specifically, PC1 represents the variation from high Co-Ni, low Ag-(Pb) values to high Ag-(Pb), low Co-Ni values. The near overlap of the Co and Ni arrows (Fig. 15) indicate that Co and Ni are proportional in the entire dataset, a feature observed in the scatterplot shown in Figure 11A. The same is true for Ag and Pb when considering BDL data (Fig. 15D). Noting that, in general, pyrite-I data are clustered to the right in the biplots and pyrite-III data are concentrated to the left, we infer that the variation represented by PC1 is directly related to a change in pyrite depositional conditions, from vigorous boiling to gentle boiling or non-boiling conditions. Considering this, and since PC1 is associated with the maximum variance of the dataset, these results indicate that high Ag values, in relation to Co and Ni, are key geochemical fingerprints of

pyrite precipitated under vigorous boiling conditions. In contrast, high Co and Ni contents with respect to Ag correspond to pyrite formed under gentle boiling or non-boiling conditions.

PC2, which represents ~22% of total variance, and corresponds to the vertical axes in Figure 15A and C, is closely related to Cu in both PCA, and also to Pb when excluding BDL data. The Cu arrow is predominantly oriented towards the pyrite-I group, in agreement with the fact that higher Cu values are related to vigorous boiling associations. Considering the PCA that includes BDL data, the near orthogonality between the Cu arrow and the Ag and Pb arrows suggest that Cu variance is almost uncorrelated to Ag and Pb variance. However, this is not the case for the PCA that excludes BDL data, where PC2 represents the variation from high Cu, low Pb values to high Pb, low Cu values, both end-members linked to vigorous boiling. We suggest then that Cu and Ag-(Pb) enrichment in pyrite are two compositional end-members, formed by similar processes, i.e., vigorous boiling. The processes leading to the development of these end-members are unclear, but differences in original fluid composition, as well as differences in how Cu-complexes and Ag-complexes are destabilized in a vigorous boiling scenario, might account for this observation.

As, on the other hand, varies almost independently of the main Co vs. Ag boiling trend (PC1), and it is closely related to PC3 (~20% of total variance), which corresponds to the vertical axes in Figure 15B and D. This metalloid, as shown previously, seems to be relatively enriched in pyrite formed under both boiling and non-boiling conditions.

4.4 Pyrite as a vector to mineralization in low- to intermediate-sulfidation epithermal systems

The precipitation of Au and Ag in low- to intermediate-sulfidation epithermal systems has long been attributed to boiling of metal-rich hydrothermal fluids (Seward, 1989; Spycher and Reed, 1989; Simmons et al., 2005; Williams-Jones et al., 2009; Pokrovski et al., 2013; Seward et al., 2014; Moncada et al., 2017). In these systems, Au-Ag mineralization concentrates preferentially in veins together with pyrite, adularia and quartz, associated with boiling levels. In this study, we have demonstrated that the systematic correlation between trace element chemistry and micro-texture in pyrite provides key information related to the physico-chemical evolution of the hydrothermal fluids. Since the CPGS can be considered as an active analogue to fossil epithermal Au-Ag deposits (Hedenquist and Lowenstern, 1994; Simmons et al., 2005), we explore the potential of using pyrite geochemistry as a tracer of boiling, and as a complementary tool to other established methods, i.e., fluid inclusions studies and bulk rock geochemistry, to vector towards Au-Ag mineralization.

First, the Ag/Co ratio of pyrite is proposed here as a discrimination tool between boiling and non-boiling zones, as shown by PCA analyses (Fig. 15). Lower Ag/Co ratios characterize pyrite

from gentle boiling to non-boiling zones, whereas higher Ag/Co ratios are expected in pyrite from vigorous boiling zones. It is important to note that, since Ag precipitation is dramatically triggered by boiling, probably there is no smooth transition in Ag/Co ratios in pyrite between boiling and non-boiling horizons. Hence, Ag/Co ratios in pyrite should be used with caution, and for vectoring purposes we suggest that Ag/Co ratios may be employed to delimit the lower zone of boiling horizons. The use of Ag/Co ratios in pyrite should be complemented with a comprehensive characterization of pyrite micro-textures. For example, high Ag/Co ratios that are associated with pyrite textures indicating rapid precipitation, i.e., areas of clustered mineral inclusions, high porosity, and colloform overgrowths, are suggestive of boiling-dominated conditions during pyrite formation. In contrast, low Ag/Co ratios associated with more euhedral morphologies and a scarcity of inclusions and pores may reflect slower crystal growth under gentle-boiling to non-boiling conditions.

Secondly, the pyrite Sb/Pb (Fig. 11F), Bi/Pb or Tl/Pb ratios may be used to differentiate between boiling horizons and their marginal or shallower areas. Pb is not preferentially transported by uprising hydrothermal fluids after boiling in comparison to Sb, Bi and Tl, which can remain in solution (Simmons et al., 2016). Relatively high Sb/Pb, Bi/Pb and Tl/Pb ratios (e.g., ≥ 0.5 , ≥ 0.03 and ≥ 0.02 , respectively, in pyrite from the CPGS, Fig. 11F) are expected in pyrite formed from fluids that underwent boiling at deeper levels (i.e., “boiled waters”), while low to moderate ratios will mark vigorous boiling horizons. This discrimination could be useful for vectoring towards ore zones laterally and vertically, and for inferring the presence of deeper mineralized veins. Given the fact that not all boiling horizons are equally mineralized, ratios between Cu, Ag and Pb could be used for discrimination. These results agree with Baker et al. (2006) and Kouhestani et al. (2017), who showed the usefulness of Cu/Pb and Pb/Ag ratios in pyrite for vectoring to high-grade Au ore zones in low- to intermediate-sulfidation epithermal Au–Ag deposits.

It is important to note that the same horizon or level within the geothermal system or epithermal deposit can contain pyrite formed under both boiling and non-boiling conditions due to overlapping of different pyrite mineralization events. For example, pyrite formation environments may have undergone telescoping due to caldera collapse or uplift (Sillitoe, 1994). Therefore, vectoring tools as proposed above should be used with caution and detailed paragenetic and geochronological studies need to be performed to address temporality of the different pyrite-bearing assemblages. In addition, multiple mineralization events within a single system can form bonanza zones of different grades, depending on the initial concentration of metals in the mineralizing hydrothermal fluids, the duration of the event, the focalization of fluids during mineralization and

the efficiency of boiling processes. Therefore, it is fundamental that pyrite geochemical vectoring aims also at discriminating between different mineralization events. Lastly, and considering that boiling is not the only process capable of leading to economic-grade mineralization in low- to intermediate epithermal systems (e.g., cooling and fluid mixing are also relevant processes), the use of pyrite as a geochemical vector should categorize which process is more prevalent in the studied system, and adapt the interpretation of the proposed elemental ratios.

5. CONCLUDING REMARKS

Pyrite from the Cerro Pabellón Geothermal System (CPGS) is characterized by significant concentrations of base metals (Co, Ni, Cu and Pb), precious metals (Au and Ag) and metalloids (As, Sb, Se, Bi, Tl), similar to pyrite from other active geothermal systems. These elements occur in both solid solution and as mineral inclusions within pyrite, with galena, chalcopyrite and acanthite being the most common mineral inclusions. As, Cu and Co commonly display compositional zoning in pyrite grains, although these features are not detectable in every grain.

The relative temporality of pyrite-bearing assemblages and inferred mechanisms of pyrite precipitation in the CPGS were determined based on contemporaneous gangue mineral associations and textures. Results indicate that physico-chemical conditions transitioned from an initial phase of vigorous boiling to a late event of gentle boiling and non-boiling. Pyrite formed during vigorous boiling is characterized by relatively higher concentrations of As, Cu, Pb, Ag and Au, coupled with lower concentrations of Co and Ni, and by textures resulting from rapid crystallization, such as irregular grain edges and areas of clustered pores and abundant mineral inclusions. Supersaturation conditions dominated during crystallization of these pyrites, given the abundance of galena, chalcopyrite, and other micro- to nano-sized mineral inclusions. In contrast, pyrite formed under gentle boiling to non-boiling conditions is characterized by higher concentrations of Co and Ni, and lower concentrations of As, Cu, Pb, Ag and Au. Textures associated with these pyrites, formed under slower crystallization kinetics and steady physico-chemical conditions during precipitation, include aggregates of euhedral and pristine homogeneously-sized crystals with scarce mineral inclusions.

The geochemistry of pyrite from the CPGS seems to be largely controlled by the incorporation of metals and metalloids from the pyrite-forming fluids once saturation conditions are met. Therefore, the high concentrations of As, Cu, Pb, Ag and Au in pyrite formed during boiling

may be the result of the abrupt destabilization of metal and metalloid complexes due to abrupt physico-chemical changes during boiling.

Our study shows that pyrite can not only record the chemical evolution of hydrothermal fluids, as previously demonstrated by Reich et al. (2013) and Tardani et al. (2017), but also can provide critical data related to physico-chemical processes such as boiling and phase separation. Since boiling of aqueous fluids is a common phenomenon occurring in a variety of pyrite-bearing hydrothermal systems (active continental and seafloor hydrothermal systems, and porphyry Cu-Mo-(Au) and epithermal Au-Ag deposits, among others), pyrite compositional and textural features are a valuable complement for discriminating and tracking boiling events in these systems and elsewhere. Particularly, the notable relation between the chemical and micro-textural features of pyrite with its formation conditions highlights the potential of using this mineral as a vector to Au-Ag mineralization in low- to intermediate-sulfidation epithermal systems.

6. ACKNOWLEDGEMENTS

This study was funded by FONDAP project 15090013 “Centro de Excelencia en Geotermia de los Andes, CEGA”. Additional funding was provided through the MSI “Millennium Nucleus for Metal Tracing Along Subduction” (NC130065). We acknowledge Dr. Kenneth Domanik, from the Lunar and Planetary Laboratory at the University of Arizona in Tucson, and Dr. Victor Valencia for their help with EMP analyses. The LA-ICP-MS analytical work was supported by CONICYT-FONDEQUIP instrumentation grant EQM120098. N. Román thanks financial support provided by CONICYT-PFCHA/MagísterNacional/2017 – 22170335 through a M.Sc. scholarship. We thank ENEL Green Power for allowing access to sample Cerro Pabellón drill cores. Finally, we acknowledge chief editor Marc Norman and associate editor Wolfgang Bach for handling the manuscript. Daniel Gregory and an anonymous reviewer are acknowledged for their helpful comments and suggestions.

7. REFERENCES

Abraitis P. K., Patrick R. A. D. and Vaughan D. J. (2004) Variations in the compositional, textural and electrical properties of natural pyrite: a review. *International Journal of Mineral Processing* **74**, 41–59.

- Aguilera F., Tassi F., Medina E. and Vaselli O. (2006) Geothermal resource exploration in northern Chile: constraints from organic and inorganic gas composition. In *Actas XI Congreso Geológico Chileno*, Antofagasta, Chile, **2**, pp. 583–586.
- Aguilera F., Ahumada S., Mercado J. L., Piscaglia F., Renzulli A. and Tassi F. (2008) Geological survey, petrology and fluid geochemistry of the Apacheta-Aguilucho volcanoes (Andean Central Volcanic Zone, northern Chile) and their geothermal system. In *Congresso del Gruppo Nazionale di Geofisica della Terra Solida (GNGTS)*, Trieste, Italy.
- Aitchison J. (1986) *The Statistical Analysis of Compositional Data*. Chapman and Hall, London, U.K. (416pp).
- Aravena D., Muñoz M., Morata D., Lahsen A., Parada M. Á. and Dobson P. (2016) Assessment of high enthalpy geothermal resources and promising areas of Chile. *Geothermics* **59**, Part A, 1–13.
- Bajwah Z. U., Seccombe P. K. and Offler R. (1987) Trace element distribution, Co:Ni ratios and genesis of the Big Cadia iron-copper deposit, New South Wales, Australia. *Mineralium Deposita* **22**, 292–300.
- Baker T., Mustard R., Brown V., Pearson N., Stanley C., Radford N. W. and Butler I. (2006) Textural and chemical zonation of pyrite at Pajingo: A potential vector to epithermal gold veins. *Geochemistry: Exploration, Environment, Analysis* **6**, 283–293.
- Bodnar R. J., Reynolds T. J. and Kuehn C. A. (1985) Fluid-Inclusion Systematics in Epithermal Systems. *Reviews in Economic Geology* **2**, 73–97
- Browne P. R. L. (1978) Hydrothermal Alteration in Active Geothermal Fields. *Annual Review of Earth and Planetary Sciences* **6**, 229–248.
- Cook N. J. and Chryssoulis S. L. (1990) Concentrations of invisible gold in the common sulfides. *The Canadian Mineralogist* **28**, 1–16.
- Cook N. J., Ciobanu C. L. and Mao J. (2009a) Textural control on gold distribution in As-free pyrite from the Dongping, Huangtuliang and Hougou gold deposits, North China Craton (Hebei Province, China). *Chemical Geology* **264**, 101–121.
- Cook N. J., Ciobanu C. L., Pring A., Skinner W., Shimizu M., Danyushevsky L., Saini-Eidukat B. and Melcher F. (2009b) Trace and minor elements in sphalerite: A LA-ICPMS study. *Geochimica et Cosmochimica Acta* **73**, 4761–4791.

- Cook N. J., Ciobanu C. L., Meria D., Silcock D. and Wade B. (2013) Arsenopyrite-Pyrite Association in an Orogenic Gold Ore: Tracing Mineralization History from Textures and Trace Elements. *Economic Geology* **108**, 1273–1283.
- Corbett, G. and Leach, T., (1998) Southwest Pacific Rim Gold-Copper Systems: Structure, Alteration, and Mineralization. *Society of Economic Geologists Special Publication* **6** (238pp)
- Cox M. E. and Browne P. R. L. (1995) The Occurrence of Pyrrhotite in the Ngawha Geothermal System, New Zealand. *Proceedings of the New Zealand Geothermal Workshop* **17**, 35–40
- Deditius A. P. and Reich M. (2016) Constraints on the solid solubility of Hg, Tl, and Cd in arsenian pyrite. *American Mineralogist* **101**, 1451–1459.
- Deditius A. P., Utsunomiya S., Renock D., Ewing R. C., Ramana C. V., Becker U. and Kesler S. E. (2008) A proposed new type of arsenian pyrite: Composition, nanostructure and geological significance. *Geochimica et Cosmochimica Acta* **72**, 2919–2933.
- Deditius A. P., Utsunomiya S., Ewing R. C., Chryssoulis S. L., Venter D. and Kesler S. E. (2009a) Decoupled geochemical behavior of As and Cu in hydrothermal systems. *Geology* **37**, 707–710.
- Deditius A. P., Utsunomiya S., Ewing R. C. and Kesler S. E. (2009b) Nanoscale “liquid” inclusions of As-Fe-S in arsenian pyrite. *American Mineralogist* **94**, 391–394.
- Deditius A. P., Utsunomiya S., Reich M., Kesler S. E., Ewing R. C., Hough R. and Walshe J. (2011) Trace metal nanoparticles in pyrite. *Ore Geology Reviews* **42**, 32–46.
- Deditius A. P., Reich M., Kesler S. E., Utsunomiya S., Chryssoulis S. L., Walshe J. and Ewing R. C. (2014) The coupled geochemistry of Au and As in pyrite from hydrothermal ore deposits. *Geochimica et Cosmochimica Acta* **140**, 644–670.
- Dong G. and Morrison G. W. (1995) Adularia in epithermal veins, Queensland: morphology, structural state and origin. *Mineralium Deposita* **30**, 11–19.
- Dong G., Morrison G. and Jaireth S. (1995) Quartz textures in epithermal veins, Queensland; classification, origin and implication. *Economic Geology* **90**, 1841–1856.
- Fleet M. E., MacLean P. J., and Barbier J. (1989) Oscillatory-zoned As-bearing pyrite from strata-bound and stratiform gold deposits; an indicator of ore fluid evolution. *Economic Geology Monograph* **6**, 356–362.

Fleet M. E., Chryssoulis S. L., MacLean P. J., Davidson R. and Weisener C. G. (1993) Arsenian pyrite from gold deposits; Au and As distribution investigated by SIMS and EMP, and color staining and surface oxidation by XPS and LIMS. *The Canadian Mineralogist* **31**, 1–17.

Fournier R. O. (1985) The behavior of silica in hydrothermal solutions. *Reviews in Economic Geology* **2**, 45–61

Franchini M., McFarlane C., Maydagán L., Reich M., Lentz D. R., Meinert L. and Bouhier V. (2015) Trace metals in pyrite and marcasite from the Agua Rica porphyry-high sulfidation epithermal deposit, Catamarca, Argentina: Textural features and metal zoning at the porphyry to epithermal transition. *Ore Geology Reviews* **66**, 366–387.

Frelinger S. N., Ledvina M. D., Kyle J. R. and Zhao D. (2015) Scanning electron microscopy cathodoluminescence of quartz: Principles, techniques and applications in ore geology. *Ore Geology Reviews* **65**, 840–852.

Gabriel K. R. (1971) The Biplot Graphic Display of Matrices with Application to Principal Component Analysis. *Biometrika* **58**, 453–467.

GDN (2011) Estudio de Impacto Ambiental: Central Geotérmica Cerro Pabellón. Technical Report Geotérmica del Norte S.A.

Genna D. and Gaboury D. (2015) Deciphering the Hydrothermal Evolution of a VMS System by LA-ICP-MS Using Trace Elements in Pyrite: An Example from the Bracemac-McLeod Deposits, Abitibi, Canada, and Implications for Exploration. *Economic Geology* **110**, 2087–2108.

González-Partida E. (2001) Especies sulfurosas del sistema hidrotermal actual del campo geotérmico de Los Azufres, Michoacán: distribución y comportamiento isotópico. *Revista Mexicana de Ciencias Geológicas* **18-1**, 103–110.

Gregory D., Meffre S. and Large R. (2014) Comparison of metal enrichment in pyrite framboids from a metal-enriched and metal-poor estuary. *American Mineralogist* **99**, 633–644.

Gregory D. D., Large R. R., Halpin J. A., Baturina E. L., Lyons T. W., Wu S., Danyushevsky L., Sack P. J., Chappaz A., Maslennikov V. V. and Bull S. W. (2015a) Trace Element Content of Sedimentary Pyrite in Black Shales. *Economic Geology* **110**, 1389–1410.

Gregory D. D., Large R. R., Halpin J. A., Steadman J. A., Hickman A. H., Ireland T. R. and Holden P. (2015b) The chemical conditions of the late Archean Hamersley basin inferred from whole rock

and pyrite geochemistry with $\Delta^{33}\text{S}$ and $\delta^{34}\text{S}$ isotope analyses. *Geochimica et Cosmochimica Acta* **149**, 223–250.

Gregory D. D., Large R. R., Bath A. B., Steadman J. A., Wu S., Danyushevsky L., Bull S. W., Holden P. and Ireland T. R. (2016) Trace Element Content of Pyrite from the Kapaï Slate, St. Ives Gold District, Western Australia. *Economic Geology* **111**, 1297–1320.

Hedenquist J. W. and Lowenstern J. B. (1994) The role of magmas in the formation of hydrothermal ore deposits. *Nature* **370**, 519–527.

Heinrich C. A. (2007) Fluid-Fluid Interactions in Magmatic-Hydrothermal Ore Formation. *Reviews in Mineralogy and Geochemistry* **65**, 363–387.

Hough R. M., Noble R. R. P. and Reich M. (2011) Natural gold nanoparticles. *Ore Geology Reviews* **42**, 55–61.

Hulen J. B., Norton D. L., Moore J. N. and Kaspereit D. (2004) Epithermal vein-hosted and stratabound Pb-Zn mineralization in an active hydrothermal system: The southern Salton Sea geothermal field, California. *Geothermal Resources Council Transactions* **28**, 415–424.

Huston D. L., Sie S. H., Suter G. F., Cooke D. R. and Both R. A. (1995) Trace elements in sulfide minerals from eastern Australian volcanic-hosted massive sulfide deposits; Part I, Proton microprobe analyses of pyrite, chalcopyrite, and sphalerite, and Part II, Selenium levels in pyrite; comparison with $\delta^{34}\text{S}$ values and implications for the source of sulfur in volcanogenic hydrothermal systems. *Economic Geology* **90**, 1167–1196.

Jochum K. P., Willbold M., Raczek I., Stoll B. and Herwig K. (2005) Chemical Characterisation of the USGS Reference Glasses GSA-1G, GSC-1G, GSD-1G, GSE-1G, BCR-2G, BHVO-2G and BIR-1G Using EPMA, ID-TIMS, ID-ICP-MS and LA-ICP-MS. *Geostandards and Geoanalytical Research* **29**, 285–302.

Kaiser H. F. (1958) The varimax criterion for analytic rotation in factor analysis. *Psychometrika* **23**, 187–200.

Keith M., Häckel F., Haase K. M., Schwarz-Schampera U. and Klemd R. (2016) Trace element systematics of pyrite from submarine hydrothermal vents. *Ore Geology Reviews* **72**, 728–745.

Keith M., Smith D. J., Jenkin G. R. T., Holwell D. A. and Dye M. D. (2018) A review of Te and Se systematics in hydrothermal pyrite from precious metal deposits: Insights into ore-forming processes. *Ore Geology Reviews* **96**, 269–282.

Koglin N., Frimmel H. E., Lawrie Minter W. E. and Brätz H. (2010) Trace-element characteristics of different pyrite types in Mesoarchaeon to Palaeoproterozoic placer deposits. *Mineralium Deposita* **45**, 259–280.

Koseki T. and Nakashima K. (2006a) Geothermal structure and feature of sulfide minerals of the Mataloko geothermal field, Flores Island, Indonesia. *Proceedings of the Asian Geothermal Symposium* **7**, 105–109.

Koseki T. and Nakashima K. (2006b) Sulfide minerals and sulfur isotope compositions from wells MT-and MT-in the Bajawa Geothermal Field, Flores Island, Indonesia. *Journal of the Geothermal Research Society of Japan* **28**, 223–236.

Kouhestani H., Ghaderi M., Large R. R. and Zaw K. (2017) Texture and chemistry of pyrite at Chah Zard epithermal gold–silver deposit, Iran. *Ore Geology Reviews* **84**, 80–101.

Kouzmanov K. and Pokrovski G. S. (2012) Hydrothermal Controls on Metal Distribution in Porphyry Cu (-Mo-Au) Systems. *Society of Economic Geologists Special Publication* **16**, 573–618

Krupp R. E. and Seward T. M. (1987) The Rotokawa geothermal system, New Zealand; an active epithermal gold-depositing environment. *Economic Geology* **82**, 1109–1129.

Large R. R., Maslennikov V. V., Robert F., Danyushevsky L. V. and Chang Z. (2007) Multistage Sedimentary and Metamorphic Origin of Pyrite and Gold in the Giant Sukhoi Log Deposit, Lena Gold Province, Russia. *Economic Geology* **102**, 1233–1267.

Large R. R., Danyushevsky L., Hollit C., Maslennikov V., Meffre S., Gilbert S., Bull S., Scott R., Emsbo P., Thomas H., Singh B. and Foster J. (2009) Gold and Trace Element Zonation in Pyrite Using a Laser Imaging Technique: Implications for the Timing of Gold in Orogenic and Carlin-Style Sediment-Hosted Deposits. *Economic Geology* **104**, 635–668.

Large R. R., Halpin J. A., Danyushevsky L. V., Maslennikov V. V., Bull S. W., Long J. A., Gregory D. D., Lounejeva E., Lyons T. W., Sack P. J., McGoldrick P. J. and Calver C. R. (2014) Trace element content of sedimentary pyrite as a new proxy for deep-time ocean–atmosphere evolution. *Earth and Planetary Science Letters* **389**, 209–220.

Large R. R., Gregory D. D., Steadman J. A., Tomkins A. G., Lounejeva E., Danyushevsky L. V., Halpin J. A., Maslennikov V., Sack P. J., Mukherjee I., Berry R. and Hickman A. (2015) Gold in the oceans through time. *Earth and Planetary Science Letters* **428**, 139–150.

- Libbey R. B. and Williams-Jones A. E. (2016) Relating sulfide mineral zonation and trace element chemistry to subsurface processes in the Reykjanes geothermal system, Iceland. *Journal of Volcanology and Geothermal Research* **310**, 225–241.
- Libbey R. B., Williams-Jones A. E., Melosh B. L. and Backeberg N. R. (2015) Characterization of geothermal activity along the North American–Caribbean Plate boundary in Guatemala: The Joaquina geothermal field. *Geothermics* **56**, 17–34.
- Longerich H. P., Jackson S. E. and Gunther D. (1996) Laser ablation inductively coupled plasma mass spectrometric transient signal data acquisition and analyte concentration calculation. *Journal of Analytical Atomic Spectrometry* **11**, 899–904.
- Maddox L. M., Bancroft G. M., Scaini M. J. and Lorimer J. W. (1998) Invisible gold; comparison of Au deposition on pyrite and arsenopyrite. *American Mineralogist* **83**, 1240–1245.
- Maslennikov V. V., Maslennikova S. P., Large R. R. and Danyushevsky L. V. (2009) Study of Trace Element Zonation in Vent Chimneys from the Silurian Yaman-Kasy Volcanic-Hosted Massive Sulfide Deposit (Southern Urals, Russia) Using Laser Ablation-Inductively Coupled Plasma Mass Spectrometry (LA-ICPMS). *Economic Geology* **104**, 1111–1141.
- Maslennikov V. V., Maslennikova S. P., Large R. R., Danyushevsky L. V., Herrington R. J., Ayupova N. R., Zaykov V. V., Lein A. Y., Tseluyko A. S., Melekestseva I. Y. and Tessalina S. G. (2017) Chimneys in Paleozoic massive sulfide mounds of the Urals VMS deposits: Mineral and trace element comparison with modern black, grey, white and clear smokers. *Ore Geology Reviews* **85**, 64–106.
- Maza S. N., Collo G., Morata D., Lizana C., Camus E., Taussi M., Renzulli A., Mattioli M., Godoy B., Alvear B., Pizarro M., Ramírez C. and Rivera G. (2018) Clay mineral associations in the clay cap from the Cerro Pabellón blind geothermal system, Andean Cordillera, Northern Chile. *Clay Minerals* **53**, 117–141.
- McKibben M. A. and Elders W. A. (1985) Fe-Zn-Cu-Pb mineralization in the Salton Sea geothermal system, Imperial Valley, California. *Economic Geology* **80**, 539–559.
- McKibben M. A., Andes J. P. and Williams A. E. (1988a) Active ore formation at a brine interface in metamorphosed deltaic lacustrine sediments; the Salton Sea geothermal system, California. *Economic Geology* **83**, 511–523.

McKibben M. A., Eldridge C. S. and Williams A. E. (1988b) Sulfur and base metal transport in the Salton Sea geothermal system. *Geothermal Resources Council Transactions* **12**, 121–125.

Meffre S., Large R. R., Steadman J. A., Gregory D. D., Stepanov A. S., Kamenetsky V. S., Ehrig K. and Scott R. J. (2016) Multi-stage enrichment processes for large gold-bearing ore deposits. *Ore Geology Reviews* **76**, 268–279.

Melekestseva I. Y., Maslennikov V. V., Tret'yakov G. A., Nimis P., Beltenev V. E., Rozhdestvenskaya I. I., Maslennikova S. P., Belogub E. V., Danyushevsky L., Large R., Yuminov A. M. and Sadykov S. A. (2017) Gold- and Silver-Rich Massive Sulfides from the Semenov-2 Hydrothermal Field, 13°31.13'N, Mid-Atlantic Ridge: A Case of Magmatic Contribution? *Economic Geology* **112**, 741–773.

Mercado J. L., Ahumada S., Aguilera F., Medina E. and Renzulli A. (2009) Geological and Structural Evolution of Apacheta-Aguilucho Volcanic Complex (AAVC), Northern Chile. In *Actas XII Congreso Geológico Chileno*, Santiago, Chile (S7:002).

Migdisov A. A., Zezin D. and Williams-Jones A. E. (2011) An experimental study of Cobalt (II) complexation in Cl^- and H_2S -bearing hydrothermal solutions. *Geochimica et Cosmochimica Acta* **75**, 4065–4079.

Migdisov A. A., Bychkov A. Y., Williams-Jones A. E. and van Hinsberg V. J. (2014) A predictive model for the transport of copper by HCl-bearing water vapour in ore-forming magmatic-hydrothermal systems: Implications for copper porphyry ore formation. *Geochimica et Cosmochimica Acta* **129**, 33–53.

Mikhlin Y., Romanchenko A., Likhatski M., Karacharov A., Erenburg S. and Trubina S. (2011) Understanding the initial stages of precious metals precipitation: Nanoscale metallic and sulfidic species of gold and silver on pyrite surfaces. *Ore Geology Reviews* **42**, 47–54.

Moncada D., Mutchler S., Nieto A., Reynolds T. J., Rimstidt J. D. and Bodnar R. J. (2012) Mineral textures and fluid inclusion petrography of the epithermal Ag–Au deposits at Guanajuato, Mexico: Application to exploration. *Journal of Geochemical Exploration* **114**, 20–35.

Moncada D., Baker D. and Bodnar R. J. (2017) Mineralogical, petrographic and fluid inclusion evidence for the link between boiling and epithermal Ag–Au mineralization in the La Luz area, Guanajuato Mining District, México. *Ore Geology Reviews* **89**, 143–170.

Muntean, J.L., Cline, J.S., Simon, A.C., and Longo, A.A., (2011). Magmatic–hydrothermal origin of Nevada’s Carlin-type gold deposits. *Nature Geoscience* **4**, 122–127.

Palenik C. S., Utsunomiya S., Reich M., Kesler S. E., Wang L. and Ewing R. C. (2004) “Invisible” gold revealed: Direct imaging of gold nanoparticles in a Carlin-type deposit. *American Mineralogist* **89**, 1359–1366.

Paton C., Hellstrom J., Paul B., Woodhead J. and Hergt J. (2011) Iolite: Freeware for the visualisation and processing of mass spectrometric data. *Journal of Analytical Atomic Spectrometry* **26**, 2508–2518.

Peterson E. C. and Mavrogenes J. A. (2014) Linking high-grade gold mineralization to earthquake-induced fault-valve processes in the Porgera gold deposit, Papua New Guinea. *Geology* **42**, 383–386.

Piscaglia F. (2012) The high temperature geothermal field of the Apacheta-Aguilucho Volcanic Complex (northern Chile): geo-petrographic surface exploration, crustal heat sources and cap-rocks. *Plinius* **38**, 148–153

Pokrovski G. S., Roux J. and Harrichoury J.-C. (2005) Fluid density control on vapor-liquid partitioning of metals in hydrothermal systems. *Geology* **33**, 657–660.

Pokrovski G. S., Borisova A. Y. and Bychkov A. Y. (2013) Speciation and Transport of Metals and Metalloids in Geological Vapors. *Reviews in Mineralogy and Geochemistry* **76**, 165–218.

Pouchou J. L. and Pichoir F. (1991) Quantitative Analysis of Homogeneous or Stratified Microvolumes Applying the Model “PAP.” In *Electron Probe Quantitation* (eds. K. F. Heinrich and D. E. Newbury). Springer, Boston, MA. pp. 31–75

Qian G., Brugger J., Testemale D., Skinner W. and Pring A. (2013) Formation of As(II)-pyrite during experimental replacement of magnetite under hydrothermal conditions. *Geochimica et Cosmochimica Acta* **100**, 1–10.

Ramírez C. and Huete C. (1981) Geología de la Hoja Ollagüe. Escala 1:250.000. *Carta Geológica de Chile* **40**. Instituto de Investigaciones Geológicas, Santiago, Chile.

Reed M. H. and Spycher N. F. (1985) Boiling, Cooling, and Oxidation in Epithermal Systems: a Numerical Modeling Approach. *Reviews in Economic Geology* **2**, 249–272

Reich M., Kesler S. E., Utsunomiya S., Palenik C. S., Chryssoulis S. L. and Ewing R. C. (2005) Solubility of gold in arsenian pyrite. *Geochimica et Cosmochimica Acta* **69**, 2781–2796.

Reich M., Utsunomiya S., Kesler S. E., Wang L., Ewing R. C. and Becker U. (2006) Thermal behavior of metal nanoparticles in geologic materials. *Geology* **34**, 1033–1036.

Reich M., Hough R. M., Deditius A., Utsunomiya S., Ciobanu C. L. and Cook N. J. (2011) Nanogeoscience in ore systems research: Principles, methods, and applications: Introduction and preface to the special issue. *Ore Geology Reviews* **42**, 1–5.

Reich M., Deditius A., Chryssoulis S., Li J.-W., Ma C.-Q., Parada M. A., Barra F. and Mittermayr F. (2013) Pyrite as a record of hydrothermal fluid evolution in a porphyry copper system: A SIMS/EMPA trace element study. *Geochimica et Cosmochimica Acta* **104**, 42–62.

Reich M., Simon A. C., Deditius A., Barra F., Chryssoulis S., Lagas G., Tardani D., Knipping J., Bilenker L., Sánchez-Alfaro P., Roberts M. P. and Munizaga R. (2016) Trace element signature of pyrite from the Los Colorados Iron Oxide-Apatite (IOA) deposit, Chile: a missing link between Andean IOA and Iron Oxide Copper-Gold systems? *Economic Geology* **111**, 743–761.

Reimann C., Filzmoser P., Garrett R. G. and Dutter R. (2008) *Statistical Data Analysis Explained: Applied Environmental Statistics with R*. John Wiley & Sons Ltd., Chichester, England (362pp)

Renzulli A., Menna M., Tibaldi A. and Flude S. (2006) New data of surface geology, petrology and Ar-Ar geochronology of the Altiplano-Puna Volcanic Complex (northern Chile) in the framework of future geothermal exploration. In *Actas XI Congreso Geológico Chileno*, Antofagasta, Chile, **2**. pp. 307–310.

Rickard D. and Luther G. W. (2007) Chemistry of Iron Sulfides. *Chemical Reviews* **107**, 514–562.

Rusk B. (2012) Cathodoluminescent Textures and Trace Elements in Hydrothermal Quartz. In *Quartz: Deposits, Mineralogy and Analytics* (eds. J. Götze and R. Möckel). Springer Berlin Heidelberg, Berlin, Heidelberg. pp. 307–329.

Rychagov S., Koroleva G., Stepanov I. and Sandimirova E. (2000) Ore Elements in the Structure of Geothermal Reservoir: Distribution, Geochemistry and Mineralogy, Probable Sources. In *Proceedings of the World Geothermal Congress 2000: Kyushu - Tohoku, Japan*. pp. 2821–2826

Rychagov S. N., Davletbaev R. G. and Kovina O. V. (2009) Hydrothermal clays and pyrite in geothermal fields: Their significance for the geochemistry of present-day endogenous processes in southern Kamchatka. *Journal of Volcanology and Seismology* **3**, 105–120.

Sánchez-Alfaro P., Reich M., Driesner T., Cembrano J., Arancibia G., Pérez-Flores P., Heinrich C. A., Rowland J., Tardani D., Lange D. and Campos E. (2016) The optimal windows for seismically-enhanced gold precipitation in the epithermal environment. *Ore Geology Reviews* **79**, 463–473.

Seward T. M. (1989) The Hydrothermal Chemistry of Gold and Its Implications for Ore Formation: Boiling and Conductive Cooling as Examples. *Economic Geology Monograph* **6**, 398–404.

Seward T. M., Williams-Jones A. E. and Migdisov A. A. (2014) 13.2 - The Chemistry of Metal Transport and Deposition by Ore-Forming Hydrothermal Fluids. In: *Treatise on Geochemistry (Second Edition)* (ed. K. K. Turekian). Elsevier, Oxford. pp. 29–57.

Shoji T., Iwano H., Kaneda H. and Takenouchi S. (1989) Trace elements in pyrite from Kirishima geothermal field and their availability for exploration. *Journal of the Geothermal Research Society of Japan* **11**, 31–42.

Shoji T., Kaneda H. and Takano Y. (1999) Minor element geochemistry in the Yanaizu-Nishiyama geothermal field, northeastern Japan. *Geothermal Resources Council Transactions* **23**, 405–406.

de Silva S. L. (1989) Altiplano-Puna volcanic complex of the central Andes. *Geology* **17**, 1102–1106.

Sillitoe R. H. (1994) Erosion and collapse of volcanoes: Causes of telescoping in intrusion-centered ore deposits. *Geology* **22**, 945–948.

Simmons S. F. and Christenson B. W. (1994) Origins of calcite in a boiling geothermal system. *American Journal of Science* **294**, 361–400.

Simmons S. F. and Browne P. R. L. (2000) Hydrothermal Minerals and Precious Metals in the Broadlands-Ohaaki Geothermal System: Implications for Understanding Low-Sulfidation Epithermal Environments. *Economic Geology* **95**, 971–999.

Simmons S. F., White N. and John D. (2005) Geological Characteristics of Epithermal Precious and Base Metal Deposits. *Economic Geology 100th Anniversary Volume*, 485–522.

Simmons S. F., Brown K. L. and Tutolo B. M. (2016) Hydrothermal Transport of Ag, Au, Cu, Pb, Te, Zn, and Other Metals and Metalloids in New Zealand Geothermal Systems: Spatial Patterns, Fluid-Mineral Equilibria, and Implications for Epithermal Mineralization. *Economic Geology* **111**, 589–618.

Simon G., Huang H., Penner-Hahn J. E., Kesler S. E. and Kao L.-S. (1999) Oxidation state of gold and arsenic in gold-bearing arsenian pyrite. *American Mineralogist* **84**, 1071–1079.

Skinner B. J., White D. E., Rose H. J. and Mays R. E. (1967) Sulfides associated with the Salton Sea geothermal brine. *Economic Geology* **62**, 316–330.

Soltani Dehnavi A., McFarlane C. R. M., Lentz D. R. and Walker J. A. (2018) Assessment of pyrite composition by LA-ICP-MS techniques from massive sulfide deposits of the Bathurst Mining Camp, Canada: From textural and chemical evolution to its application as a vectoring tool for the exploration of VMS deposits. *Ore Geology Reviews* **92**, 656–671.

Spycher N. F. and Reed M. H. (1989) Evolution of a Broadlands-type epithermal ore fluid along alternative P-T paths; implications for the transport and deposition of base, precious, and volatile metals. *Economic Geology* **84**, 328–359.

Steadman J. A., Large R. R., Meffre S., Olin P. H., Danyushevsky L. V., Gregory D. D., Belousov I., Lounejeva E., Ireland T. R. and Holden P. (2015) Synsedimentary to Early Diagenetic Gold in Black Shale-Hosted Pyrite Nodules at the Golden Mile Deposit, Kalgoorlie, Western Australia. *Economic Geology* **110**, 1157–1191.

Sykora S., Cooke D. R., Meffre S., Stephanov A. S., Gardner K., Scott R., Selley D. and Harris A. C. (2018) Evolution of Pyrite Trace Element Compositions from Porphyry-Style and Epithermal Conditions at the Lihir Gold Deposit: Implications for Ore Genesis and Mineral Processing. *Economic Geology* **113**, 193–208.

Tanner D., Henley R. W., Mavrogenes J. A. and Holden P. (2016) Sulfur isotope and trace element systematics of zoned pyrite crystals from the El Indio Au–Cu–Ag deposit, Chile. *Contributions to Mineralogy and Petrology* **171** (4), 1–17

Tardani D., Reich M., Deditius A. P., Chryssoulis S., Sánchez-Alfaro P., Wrage J. and Roberts M. P. (2017) Copper–arsenic decoupling in an active geothermal system: A link between pyrite and fluid composition. *Geochimica et Cosmochimica Acta* **204**, 179–204.

Tassi F., Aguilera F., Darrah T., Vaselli O., Capaccioni B., Poreda R. and Medina E. (2009) Geochemical survey of geothermal systems in northern Chile. In *Actas XII Congreso Geológico Chileno*, Santiago, Chile (S6:014).

- Tassi F., Aguilera F., Darrah T., Vaselli O., Capaccioni B., Poreda R. J. and Delgado Huertas A. (2010) Fluid geochemistry of hydrothermal systems in the Arica-Parinacota, Tarapacá and Antofagasta regions (northern Chile). *Journal of Volcanology and Geothermal Research* **192**, 1–15.
- Thomas H. V., Large R. R., Bull S. W., Maslennikov V., Berry R. F., Fraser R., Froud S. and Moyer R. (2011) Pyrite and Pyrrhotite Textures and Composition in Sediments, Laminated Quartz Veins, and Reefs at Bendigo Gold Mine, Australia: Insights for Ore Genesis. *Economic Geology* **106**, 1–31.
- Tossell J. A., Vaughan D. J. and Burdett J. K. (1981) Pyrite, marcasite, and arsenopyrite type minerals: Crystal chemical and structural principles. *Physics and Chemistry of Minerals* **7**, 177–184.
- Urzúa L., Powell T., Cumming W. and Dobson P. (2002) Apacheta, a New Geothermal Prospect in Northern Chile. *Geothermal Resources Council Transactions* **26**, 65–69.
- Vaughan D. J. and Craig J. R. (1978) *Mineral Chemistry of Metal Sulfides*, Cambridge University Press, Cambridge, United Kingdom.
- Vaughan J. P. and Kyin A. (2004) Refractory gold ores in Archaean greenstones, Western Australia: mineralogy, gold paragenesis, metallurgical characterization and classification. *Mineralogical Magazine* **68**, 255–277.
- Wells, J.D. and Mullens, T.E. (1973). Gold-Bearing Arsenian Pyrite Determined by Microprobe Analysis, Cortez and Carlin Gold mines, Nevada. *Economic Geology* **68**, 187–201.
- Williams-Jones A. E., Bowell R. J. and Migdisov A. A. (2009) Gold in Solution. *Elements* **5**, 281–287.
- Wilson S. A., Ridley W. I. and Koenig A. E. (2002) Development of sulfide calibration standards for the laser ablation inductively-coupled plasma mass spectrometry technique. *Journal of Analytical Atomic Spectrometry* **17**, 406–409.
- Wohlgemuth-Ueberwasser C. C., Viljoen F., Petersen S. and Vorster C. (2015) Distribution and solubility limits of trace elements in hydrothermal black smoker sulfides: An in-situ LA-ICP-MS study. *Geochimica et Cosmochimica Acta* **159**, 16–41.

FIGURE CAPTIONS

Figure 1. Location and geological characteristics of the Cerro Pabellón Geothermal System (CPGS). (A) Location of the CPGS in relation to other geothermal areas of interest (as indicated by Aravena et al., 2016) and relevant ore deposits; (B) Simplified geological map of the Cerro Pabellón geothermal field, taken from Maza et al. (2018), showing the location of the PEXAP-1 drillhole collar (red circle) and the orientation of the cross section shown in C (red dashed line). (C) Simplified conceptual model for the CPGS, showing isotherms and magnetotelluric (MT) resistivity data, taken from Urzúa et al. (2002). (D) Simplified geological profile of the PEXAP-1 well, indicating hydrothermal alteration and zones of the geothermal system as interpreted by Maza et al. (2018). The location of the pyrite-bearing samples studied in the present work is also shown.

Figure 2. Polarized reflected light (A) and backscattered electron (BSE) images (B-D) showing representative textural features of pyrite from the CPGS (Group I). Pyrite-I occurs as elongated grains associated with colloform silica and Fe-oxide bands (A, B). Porous and inclusion (galena and chalcopyrite)-rich zones are key textural features of pyrite-I (A-D). These porous zones can be elongated, following the facets of the host pyrite grains (A, B); can constitute the core of pyrite grains (C); or can be associated with fractured zones in some pyrite grains (D). Pristine pyrite areas occur in all of the grains. Late chalcopyrite can be seen in the rims of some pyrite grains (A, C, D) and also in the interstitial space between pyrite crystals (D). Cal: calcite; Ccp: chalcopyrite; Py: pyrite; Qz: quartz.

Figure 3. Backscattered electron (BSE) (A, B, D) and polarized reflected light (C) images showing representative textural features of pyrite from the CPGS (Groups II and III) and late-stage base and precious metal sulfides. Pyrite-II grains are euhedral to subhedral and have porous, inclusion-rich cores and pristine rims (A, B; inclusions: galena and acanthite). Pyrite-III, in contrast, occurs as aggregates of euhedral to subhedral grains with relatively homogeneous sizes and it shows scarce porosity and mineral inclusions than pyrite-I and II (C, D). The mineral inclusions shown in (D) precipitated after pyrite deposition, in the interstices between pyrite grains. The late base and precious metal sulfide mineralization event consists of chalcopyrite followed by galena + acanthite. Usually, this assemblage is adjacent to previous pyrite grains (C, D). A minor mode of occurrence of pyrite from the CPGS is shown in (B), where it is found replacing ilmenite lamellae in Ti-

magnetite. Ac: acanthite; Adl: adularia; Cal: calcite; Ccp: chalcopyrite; Gn: galena; Ilm: ilmenite; Mag: magnetite; Py: pyrite; Qz: quartz.

Figure 4. Backscattered electron (BSE) and cathodoluminescence (SEM-CL) images showing pyrite from CPGS in association with different veinlets; veinlet generations are arranged from the earliest (A) to the latest (E-F). (A) Pyrite from Group I (pyrite-I), associated with colloform silica + Fe-oxide crustiform bands; (B) Gangue minerals association for pyrite from Group II (pyrite-II), showing crustiform bands of colloform silica, mosaic quartz and later zoned quartz+sub-rhombic adularia; (D-E) (depicting the same area) Pyrite-II, associated with colloform silica and later zoned quartz; (E-F) (depicting the same area) Pyrite from Group III (pyrite-III), associated with sub- to euhedral, zoned quartz + sub-rhombic adularia. The brighter spots within colloform silica in (A) are due to the presence of Fe-oxides. Adl: adularia; Cal: calcite; Ccp: chalcopyrite; Chl: chlorite; Mag: magnetite; Py: pyrite; Qz: quartz.

Figure 5. Simplified paragenetic sequence of the CPGS for samples used in this study, highlighting the relative temporality of the groups of pyrite and their association with gangue minerals, and the late base- and precious metal sulfide mineralization event recorded in the samples.

Figure 6. Concentration plot for minor and trace elements in pyrite from the CPGS (samples BA20, BA21, BA27, BA30, BA31, BA33 and BA34). EMPA and LA-ICP-MS spot analysis data are included and shown as yellow-segmented lines and boxplots, respectively. Data are plotted in parts per million (ppm) on a vertical logarithmic scale. For boxplots, white color represents all available LA-ICP-MS data (n=264), while gray boxes represent inclusion-free data only (n=118). In each boxplot, minimum, median and maximum concentrations are marked, and the number of analyses above detection limit for each element is displayed inside of each box. The horizontal segmented line marks the mean detection limit (mdl) of EMP analyses for all elements.

Figure 7. Concentration boxplot for selected minor and trace elements in pyrite from Groups I, II and III. Only inclusion-free LA-ICP-MS spot analysis data were considered (n = 118). Yellow boxes represent pyrite-I, which corresponds to pyrite associated with bands of colloform silica and Fe-oxides (n = 35); blue boxes represent pyrite-II, associated with crust-like bands of colloform

silica, mosaic quartz and late zoned quartz + sub-rhombic adularia ($n = 56$); and white boxes represent pyrite-III, associated with zoned quartz + sub-rhombic adularia veinlets ($n = 27$). Data are plotted in parts per million (ppm) on a vertical logarithmic scale. In each boxplot, minimum, median and maximum concentrations are marked, and the number of analyses above detection limit for each element is shown as a number inside each box.

Figure 8. Representative micro-textures and chemical zonations of pyrite-I (Group I) from the propylitic alteration of the CPGS. Sample: BA33. (A and D): backscattered electron (BSE) images. (B, C, E and F) Qualitative, wavelength dispersive spectrometry (WDS) X-ray maps of the same grains shown in the BSE images. (B and E) As ($L\alpha$) maps; (C and F) Cu ($K\alpha$) maps. The WDS maps show zonations of As ($L\alpha$) and Cu ($K\alpha$); white arrows in (B) and (C) highlight zones where As and Cu concentrations are coupled. Cu ($K\alpha$) distributions in (C) and (F) show discrete chalcopyrite inclusions, and additionally in (C), late chalcopyrite in fractures of pyrite grains. A color scale bar is shown for each WDS map. Ccp: chalcopyrite; Gn: galena; Py: pyrite.

Figure 9. Representative microtextures and chemical zonations of pyrite-II (Group II) from the propylitic alteration of the CPGS. Samples: BA21 (first and second row) and BA31 (third row). (A, E, and I) backscattered electron (BSE) images showing pyrite grains. All other images are qualitative wavelength dispersive spectrometry (WDS) X-ray maps of areas shown in the BSE images. (B, F, and J) As ($L\alpha$) maps; (C, G, and K) Cu ($K\alpha$) maps; (D, H, and L) Co ($K\alpha$) maps. The WDS maps show zonation of As ($L\alpha$), Cu ($K\alpha$) and Co ($K\alpha$). Cu ($K\alpha$) distributions in (C) and (K) show discrete inclusions of chalcopyrite. Discrete galena and chalcopyrite inclusions are visible in the BSE images. A color scale bar for intensity is shown in each WDS map, and selected EMP analyses for As and Cu are included as reference (red crosses). Ccp: chalcopyrite; Gn: galena; Py: pyrite.

Figure 10. Representative micro-textures and chemical zonations of pyrite-III (Group III) from the propylitic alteration of the CPGS. Sample: BA20. (A and E) backscattered electron (BSE) images showing pyrite grains. All other images are qualitative wavelength dispersive spectrometry (WDS) X-ray maps of areas shown in the BSE images. (B and F) As ($L\alpha$) maps; (C and G) Cu ($K\alpha$) maps; (D and H) Co ($K\alpha$) maps. The WDS maps show relatively homogeneous concentrations of As ($L\alpha$),

Cu ($K\alpha$) and Co ($K\alpha$) in pyrite, and highlight the relatively higher concentration of Cu and Co in galena and achantite in relation to pyrite. Ac: acanthite; Ccp: chalcopyrite; Gn: galena; Py: pyrite.

Figure 11. Elemental concentration scatterplots in pyrite from the CPGS (inclusion-free LA-ICP-MS data only, $n = 118$): (A) Co vs. Ni; (B) Co vs. Cu; (C) Co vs. As; (D) Au vs. As; (E) Cu vs. As; (F) Sb vs. Pb; (G) Ag vs. Pb; (H) Bi vs. Sb; (I) Tl vs. Sb. In (A), (F), (G), (H) and (I), the dashed lines represent different elements ratios for reference. The dashed curve in (D) represents solubility limit of Au as a function of As concentrations, as determined by Reich et al. (2005). All concentrations are in parts per million (ppm).

Figure 12. As-Fe-S composition of pyrite from the CPGS. Only EMPA data were considered. $n = 264$. (A) Ternary diagram showing the As-Fe-S composition of pyrite. Five different trends show substitution of (i) As for S (As^1 -pyrite); (ii) As^0 nano-inclusions (Deditius et al., 2009a); (iii) As^{2+} for Fe (As^{2+} -pyrite, Qian et al., 2013); (iv) As^{3+} for Fe (As^{3+} -pyrite, Deditius et al., 2008); and divalent metals (Me^{2+}) substituting isovalently for Fe. The composition for As^{2+} -pyrite (after Qian et al., 2013; Deditius et al., 2014) was calculated based on the assumption of ideal occupancy of S (66.66 mol %). The dashed gray arrow marks a trend, parallel to the As^0 nano-inclusions trend, displayed by a subgroup of the dataset. This deficiency in S and Fe concentration is interpreted as the presence of As^0 nano-inclusions. (B) As vs. S scatterplot, showing the inverse correspondence between these elements in pyrite from the CPGS. Yellow circles: pyrite-I, blue symbols: pyrite-II, and white circles, pyrite-III. Correlation coefficients are also shown ($r_P =$ Pearson, $r_S =$ Spearman).

Figure 13. Representative LA-ICP-MS depth-concentration profiles (time vs. intensity) of selected isotopes in pyrite from the CPGS. (A) Backscattered electron (BSE) image of a pyrite grain in sample BA20, showing the location of spot analysis BA20-6-6 (30 μm). (B) (Pyrite-III) Depth-concentration profile of spot analysis BA20-6-6, where the presence of individual galena and Au + Ag mineral particles (or a cluster) are identified by coupled ^{208}Pb and ^{209}Bi , and ^{107}Ag and ^{197}Au peaks, respectively. (C) (Pyrite-II) Flat signal for the investigated isotopes suggests incorporation as solid solution into pyrite or nanoparticles not resolved in the LA-ICP-MS depth-concentration profiles. (D) (Pyrite-I) Cu-bearing inclusions as seen in depth profiles, together with an Au-Ag-bearing inclusion. (E) (Pyrite-III) Ag-Se-bearing inclusions as seen in depth profiles. In this case, it occurs together with Ag and galena inclusions. (F) (Pyrite-II) flat signals for the isotopes

represented, including Tl and Hg signals. In (C), the slight increase in ^{107}Ag and ^{197}Au intensities with time may be related to a higher concentration of Ag and Au in depth.

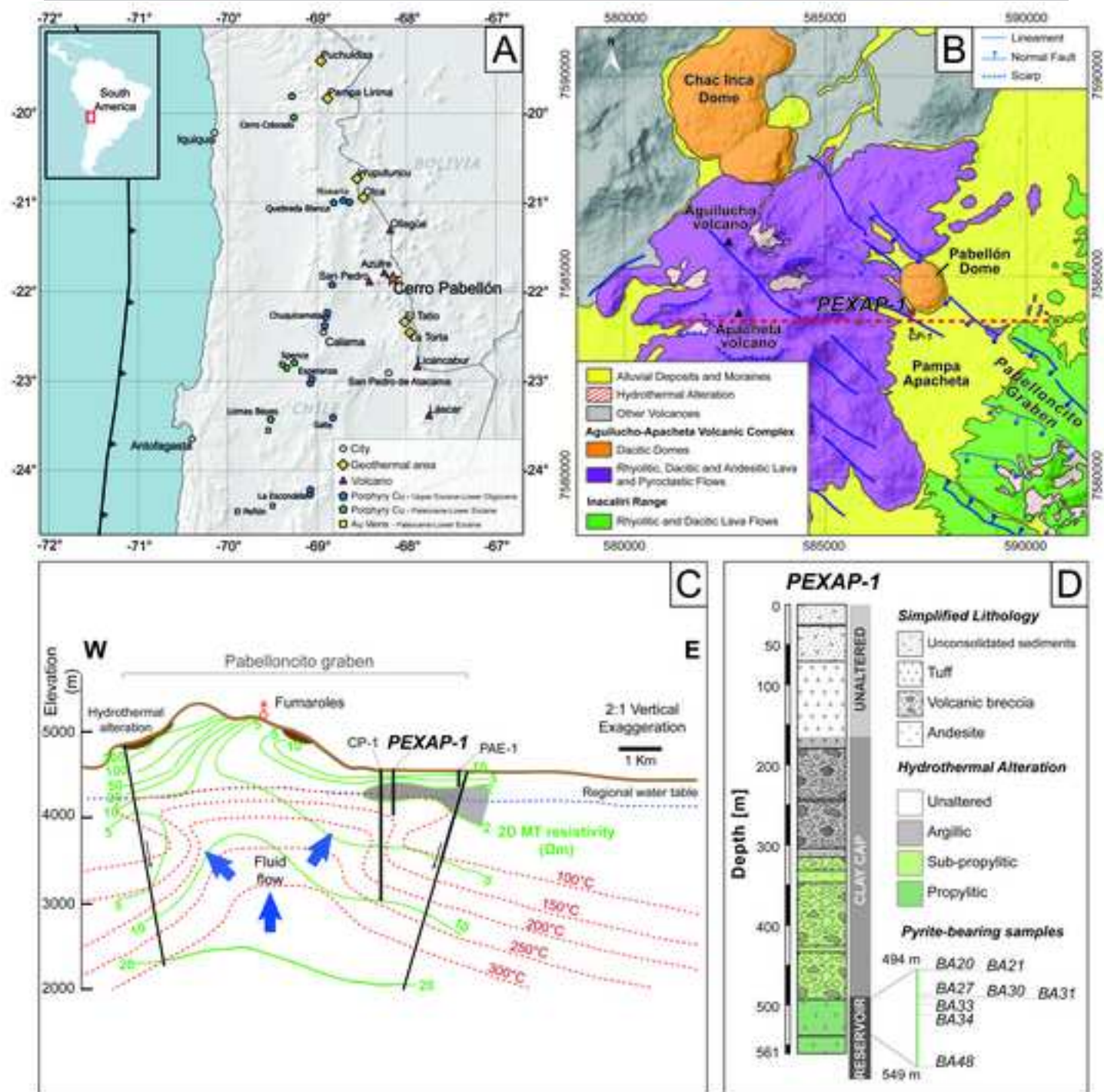
Figure 14. Plot of Co and Ni concentrations in pyrite from the CPGS and other active geothermal systems. Data symbols for CPGS samples are the same as used in Figure 11.

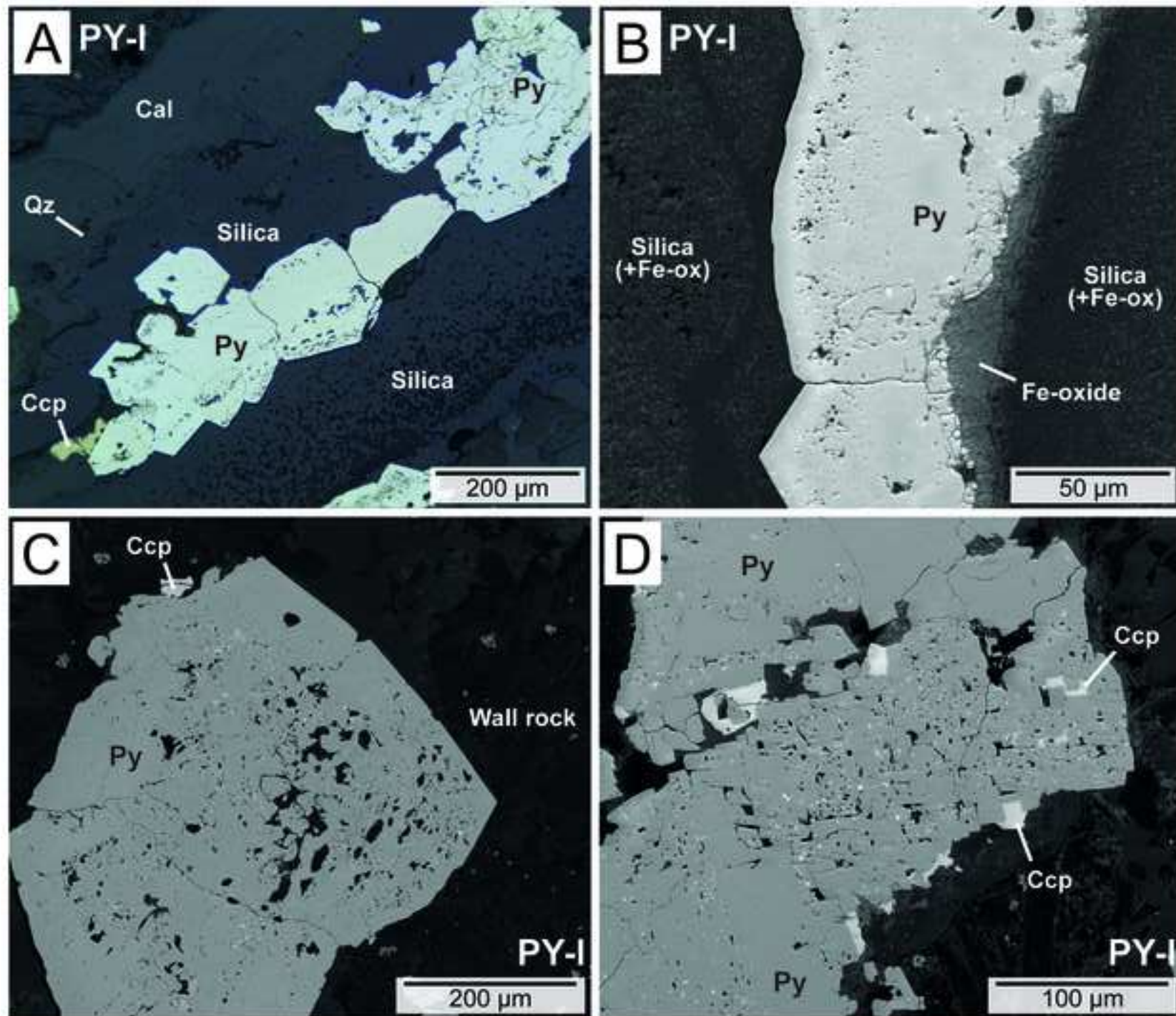
Figure 15. Biplots for Varimax-rotated Principal Component Analysis (PCA) of CLR-transformed pyrite concentrations. Only inclusion-free LA-ICP-MS data on Co, Ni, As, Cu, Ag and Pb were used. Bottom and left axes in every plot display the loadings of the Principal Components (PC), which are to be read considering the arrows (analyzed elements). The percentage shown on the axes represents the total variance explained by that component. Top and right axes show the scores of the PCs, which are associated to the points (individual analyses). (A) and (B) shows PCA performed without data below detection limit, and (C) and (D) shows a PCA where data below detection were replaced for a concentration equal to half of the detection limit. In both PCA, more than 80% of the total variance can be represented with the extraction of three PCs. (A and C) PC1 vs. PC2; (B and D) PC1 vs. PC3. In each biplot, the pyrite genetic interpretation is given (vigorous boiling vs. gentle boiling to non-boiling conditions). The * symbol denotes that the variables considered here were log-transformed and standardized (calculation of Z-values) prior to PCA, as described in the Methodology section, and do not correspond to raw compositional data.

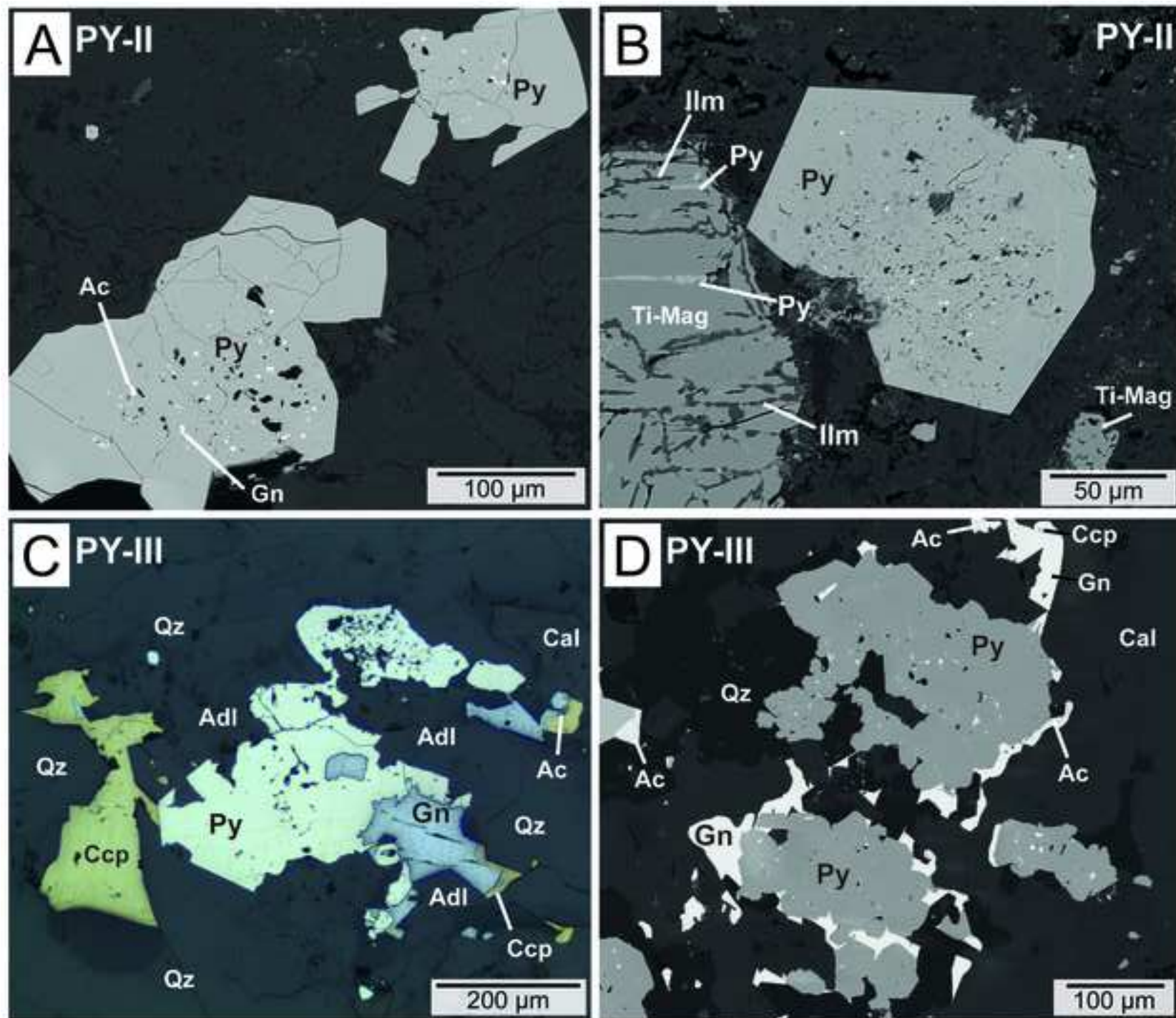
Figure 1

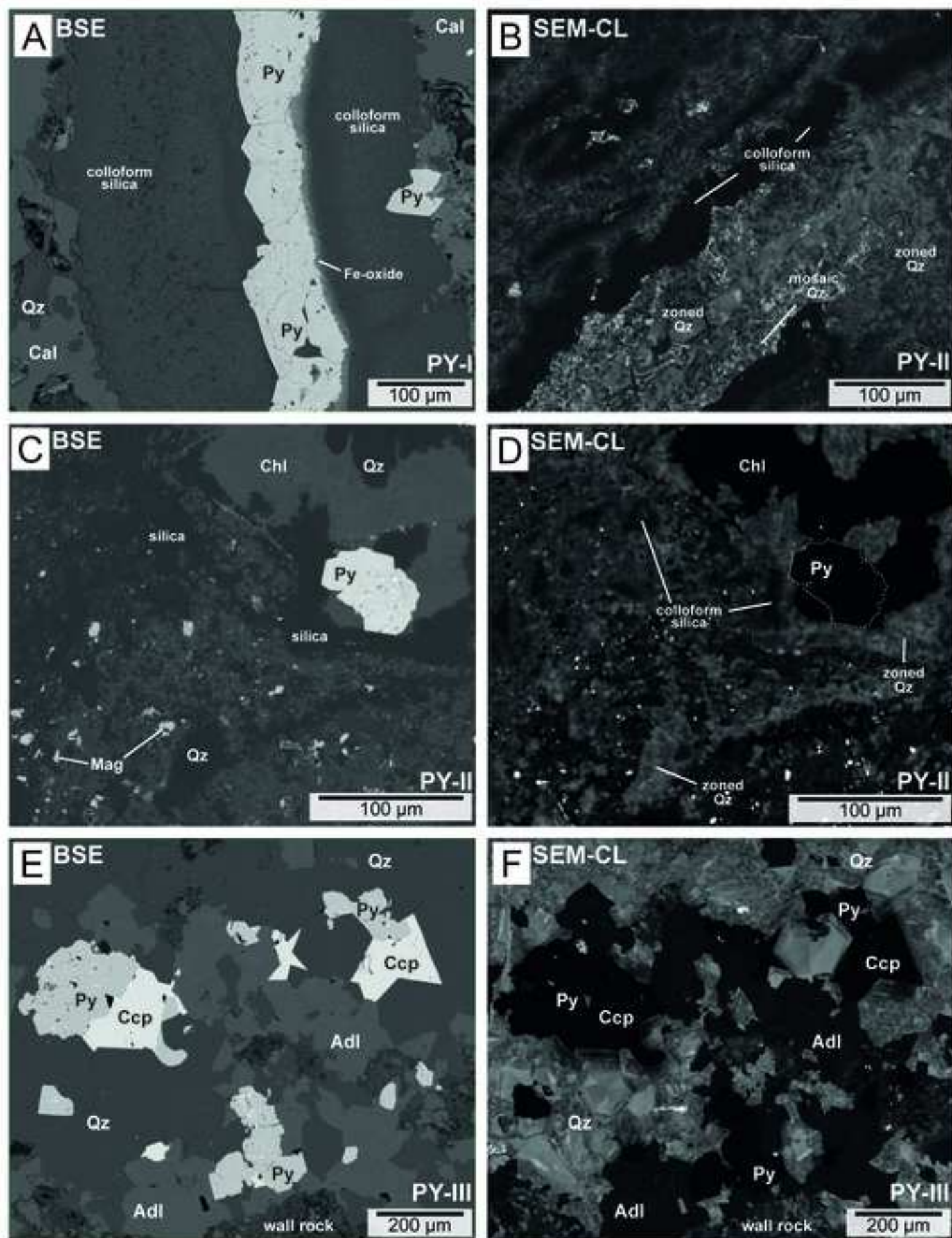
[Click here to download high resolution image](#)

ACCEPTED MANUSCRIPT









		Pyrite stage	Cu-Ag-Pb sulfide stage
Gangue minerals	<i>colloform silica</i>	—————	
	<i>Fe-oxide</i>	—————	
	<i>quartz (mosaic)</i>	—————	
	<i>quartz (zoned)</i>	—————	
	<i>adularia (sub-rhombic)</i>	—————	
	<i>calcite (rhombic)</i>		—————
Sulfides	<i>pyrite (Group-I)</i>	————— <i>py-I</i>	
	<i>pyrite (Group-II)</i>	————— <i>py-II</i>	
	<i>pyrite (Group-III)</i>	————— <i>py-III</i>	
	<i>chalcopyrite</i>	----- <i>as inclusions in py</i>	—————
	<i>galena</i>	----- <i>as inclusions in py</i>	—————
	<i>acanthite</i>	-----	—————

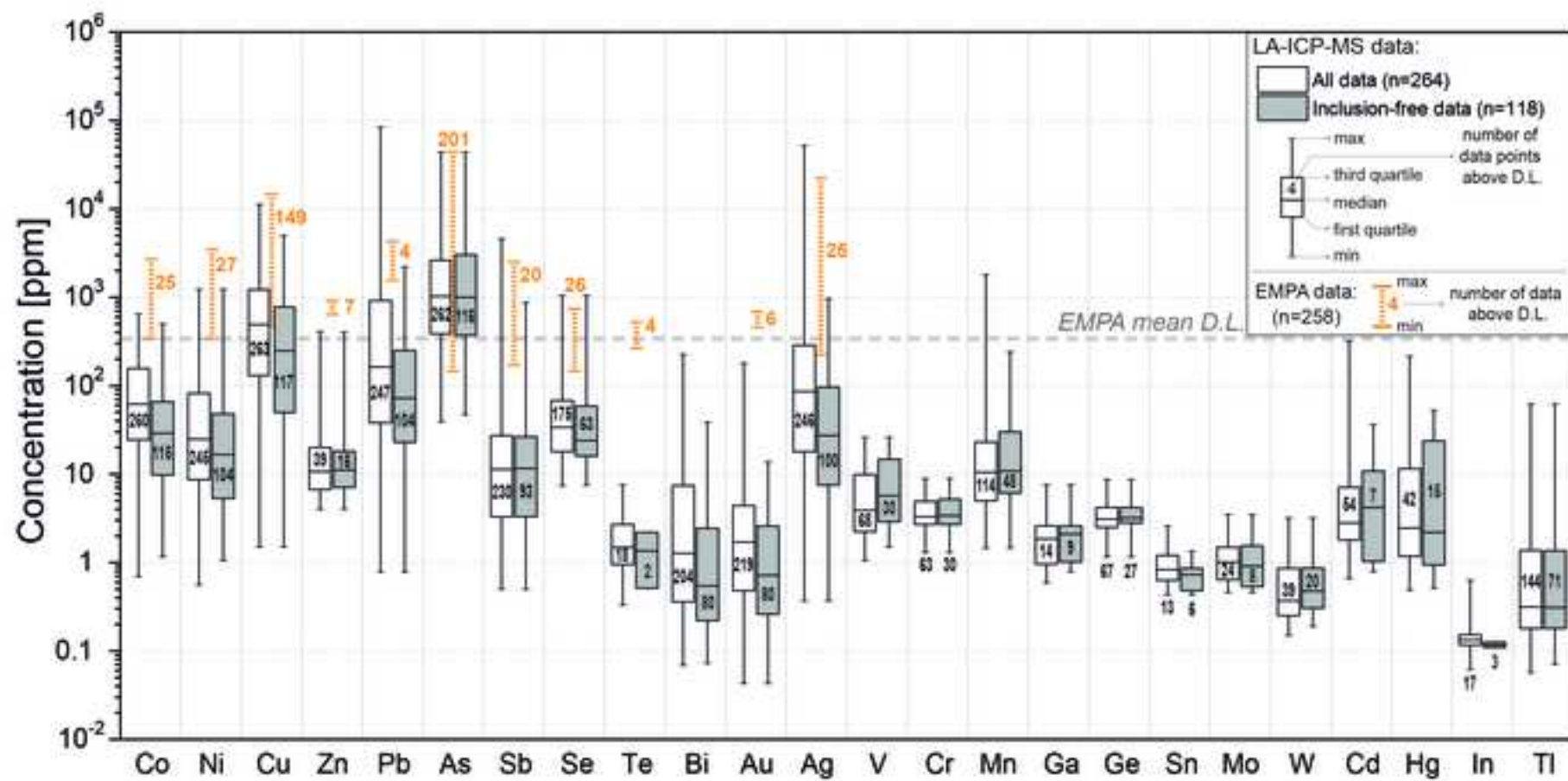
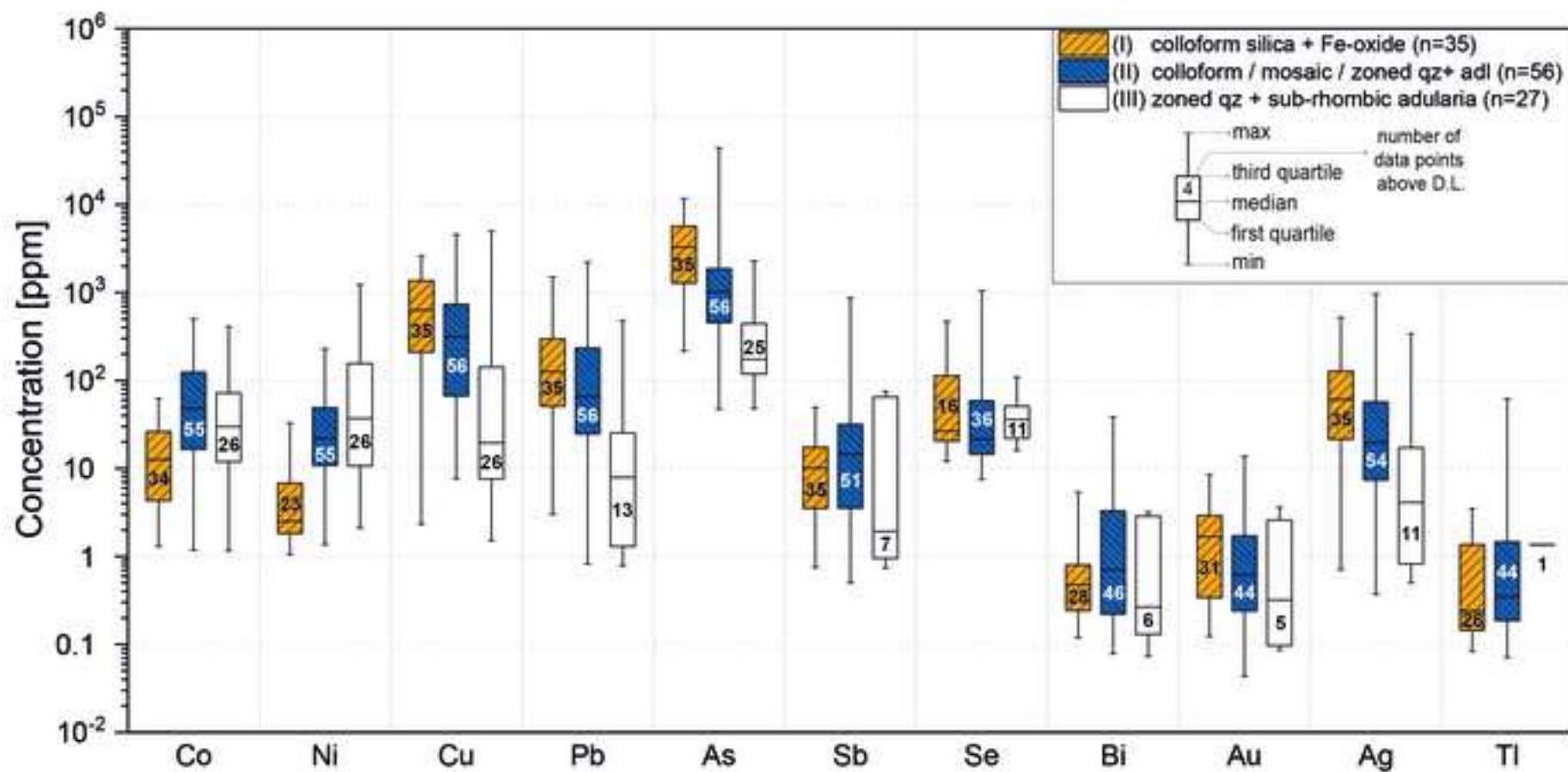
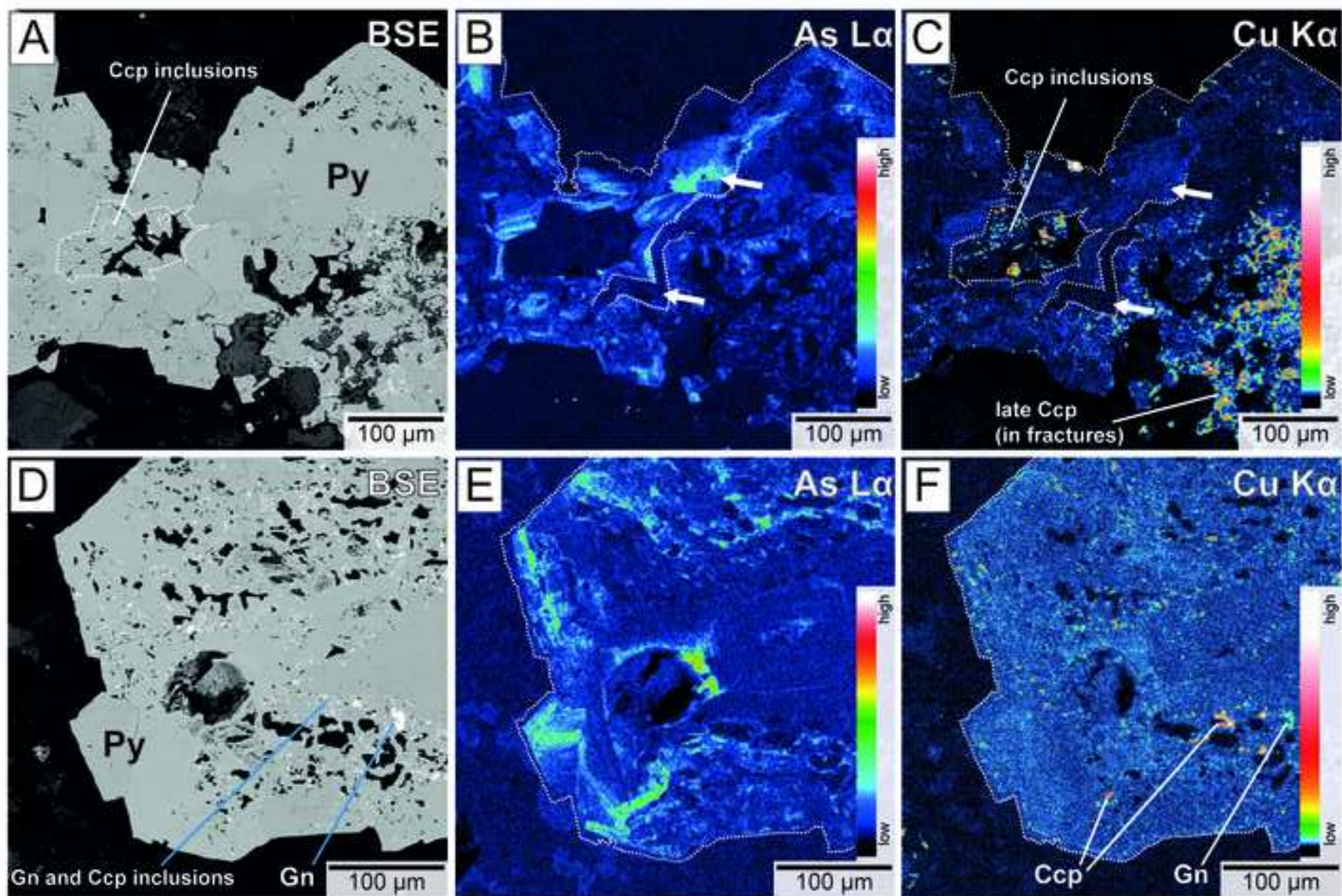
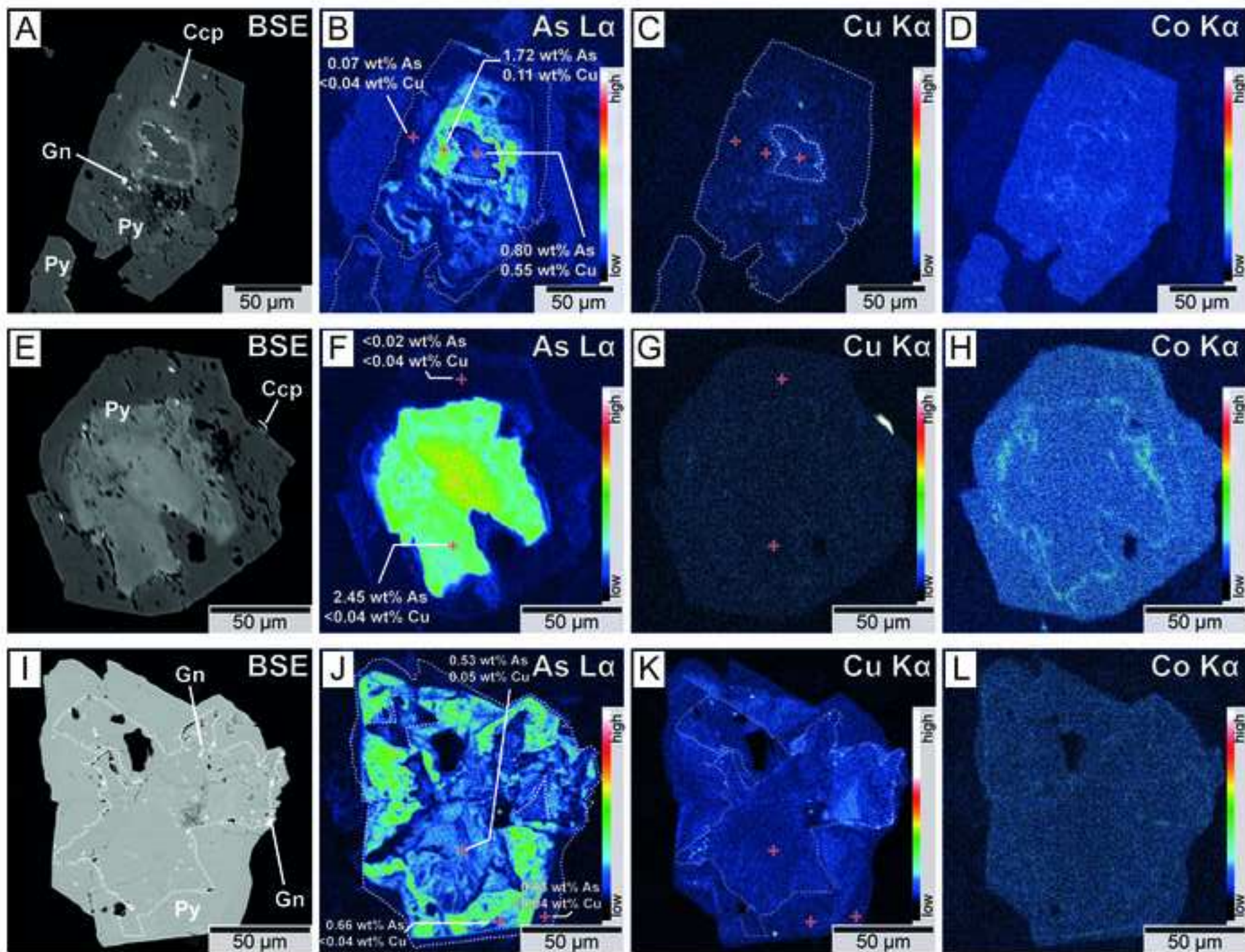
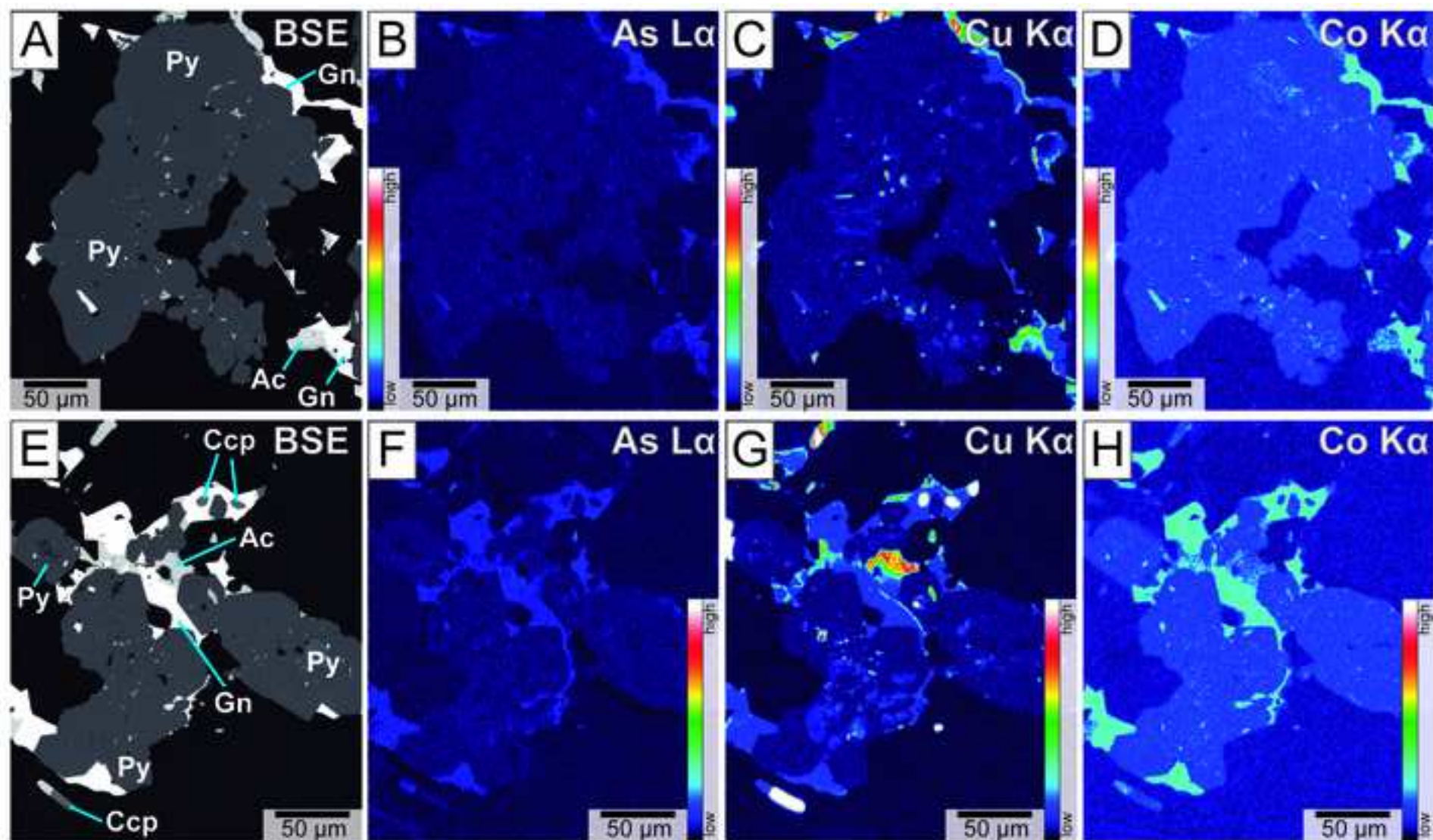


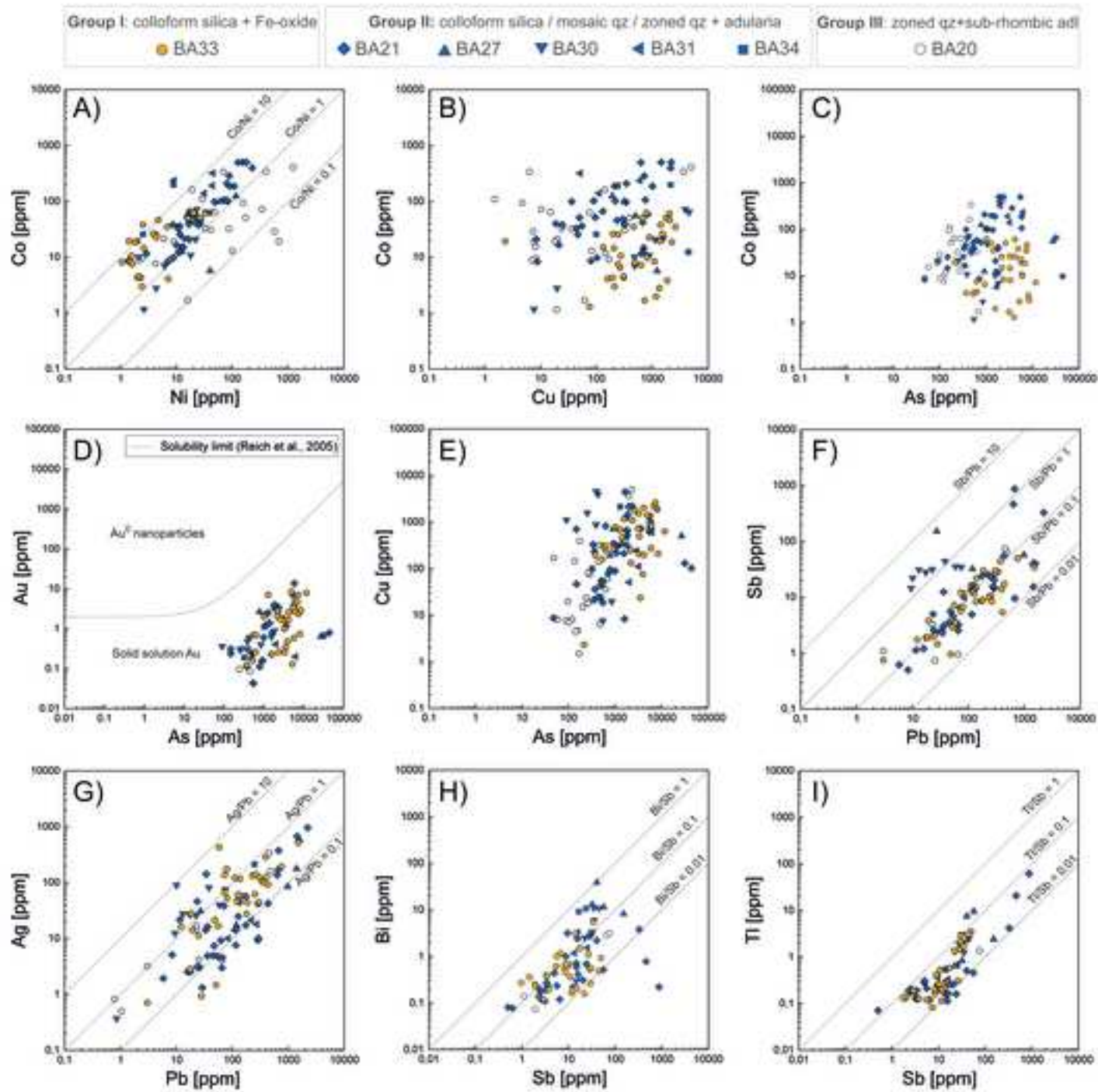
Figure 7

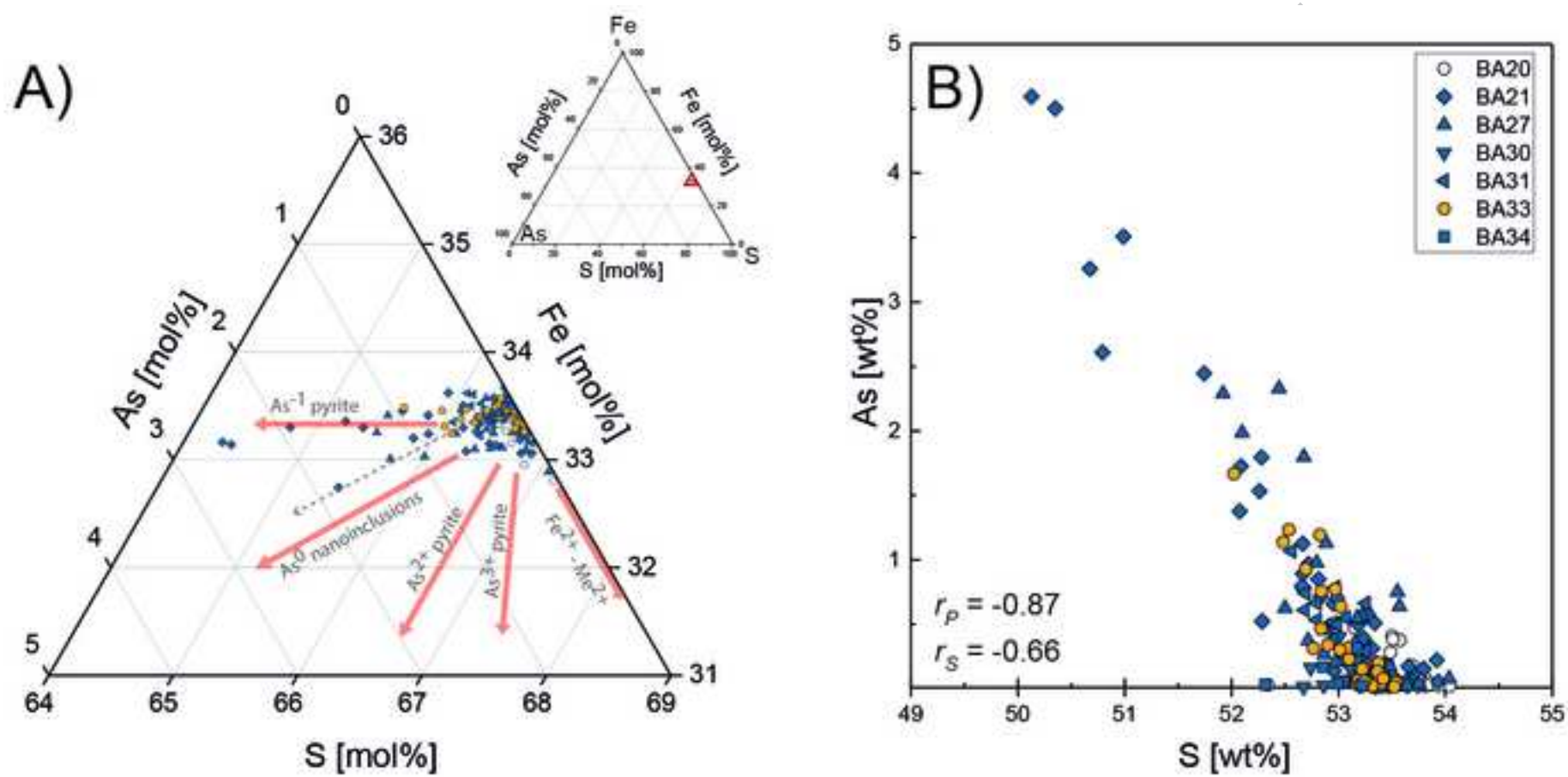












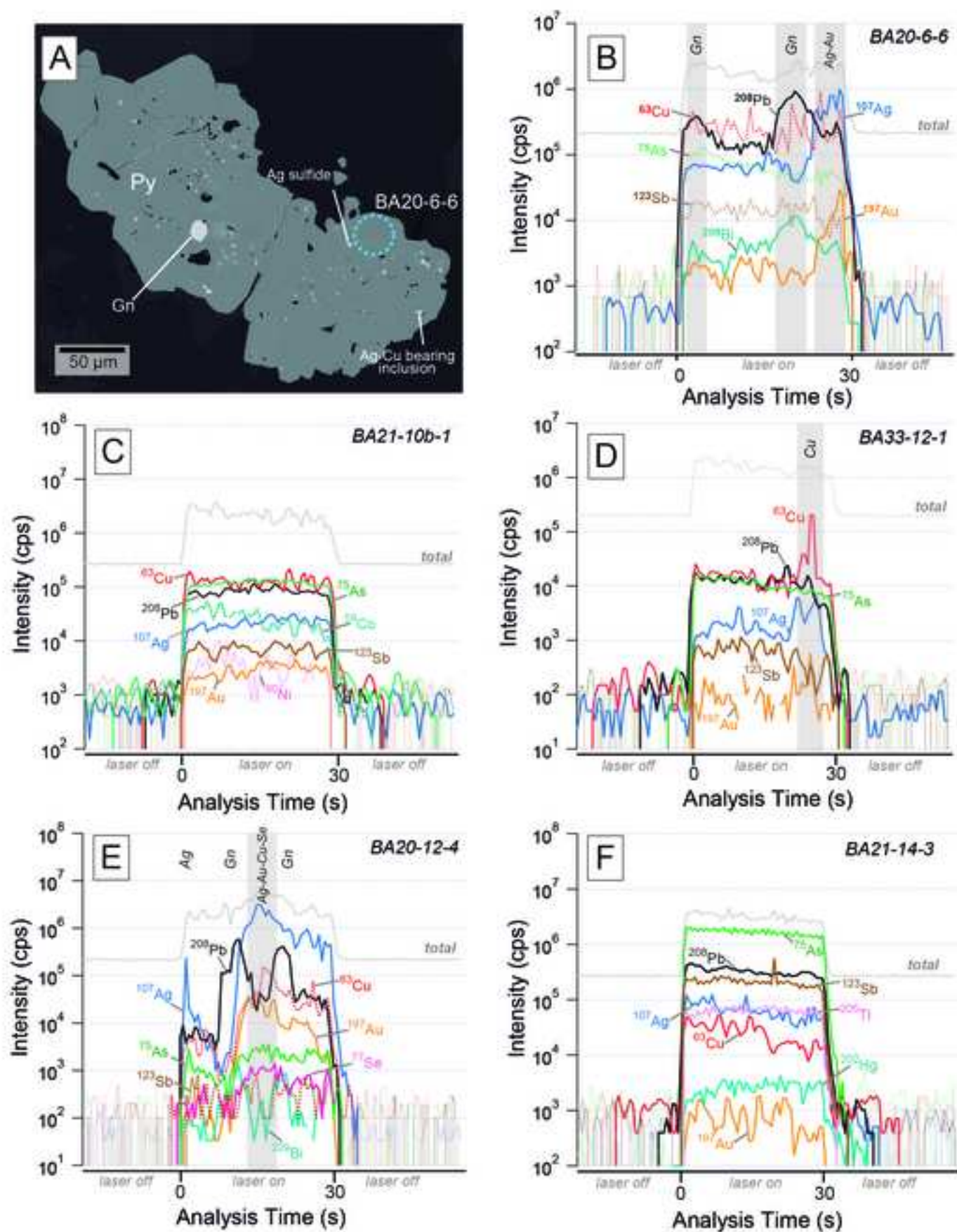


Figure 14

